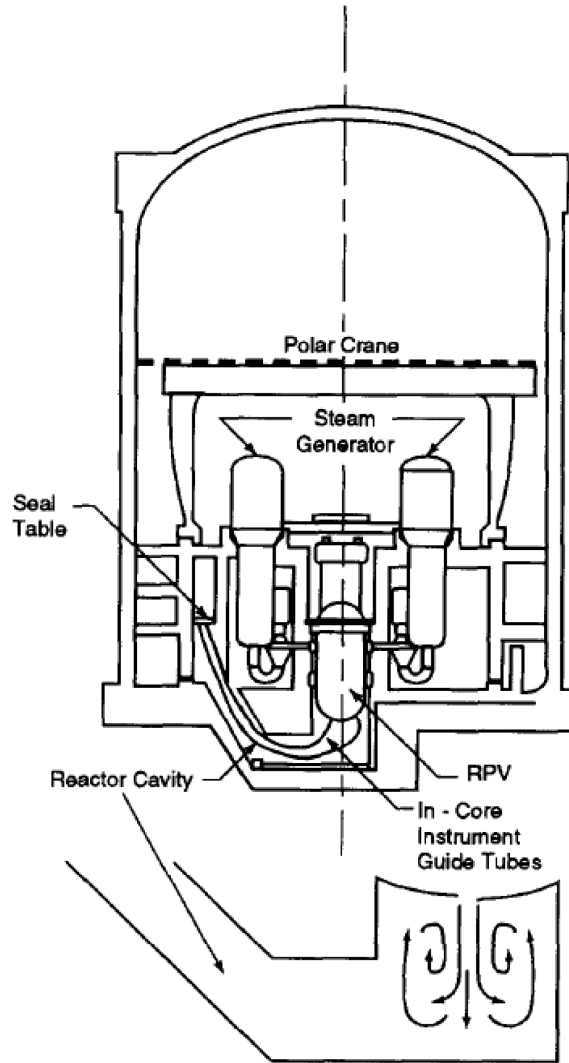


## 21A VERIFICATION OF THE TRANSIENT CLCH MODEL

In this Appendix, the transient CLCH model is verified with a sample of three experiments from the Integral Effects Tests (IET) series. This adds to the previous extensive validation of the original CLCH model that captured only the final state. The tests were scaled to typical PWR conditions, including the preservation (linearly scaled) of the key geometric features (see Figures 21A-1 and 21A-2), especially with respect to the cavity and the so-called intermediate compartment. The IET tests were conducted in counterparts at two scales: at 1/10-scale in the SURTSEY facility at Sandia National Laboratories (SNL) (Allen et al., 1994), and at 1/40-scale in the COREXIT facility at Argonne National Laboratory (ANL) (Binder et al., 1994). Two ANL tests (IET-1RR and IET-8) and one SNL test (IET-1) were selected for interpretation here—they were conducted in inert atmospheres as is appropriate to the present application.

The CLCH model reflects thermal/chemical equilibrium in the melt dispersal (flow) process, and separation of the melt out of this 'equilibrium stream' in the intermediate compartment. The "analysis domain" consists of two major compartments: the "vessel" which represents the containment in the plant geometry, and the "sub-compartment" which represents the intermediate volume (see a schematic representation in Figure 21A-3). By solving a system of mass and energy balance equations for these compartments, we can obtain the dynamics of pressurization in the "vessel". This extension of the model to capture the transient is straightforward, and the complete formulation can be found in Table 21.3.4.3-1 of Section 21.3.4.3 in the main body of the report.

The model implementation to these particular tests considered here was done in terms of the definition of conditions given in Table 21A-1. The parameters utilized are summarized in Table 21A-2. The melt entrainment time was obtained from the CLCH model correlation, and the oxidation efficiency too is from this previous work with CLCH. The ejection time quoted in Table 21A-2 is from the experimental data and reflects the transition period from melt ejection to pure steam blowdown. While unimportant in the previous applications of CLCH, it is important here in our interest to capture the complete transient. As seen in Figure 21A-4, the pure blowdown portion is predictable by a straightforward isentropic expansion. The blowdown rate used for the transition period was approximated in the manner as shown in the figure.



**Figure 21A-1. The Containment Geometry Considered in the IET tests**

The containment geometry considered in the IET tests and an illustration of the recirculation flow pattern in the cavity (adapted from Yan and Theofanous (1996)).

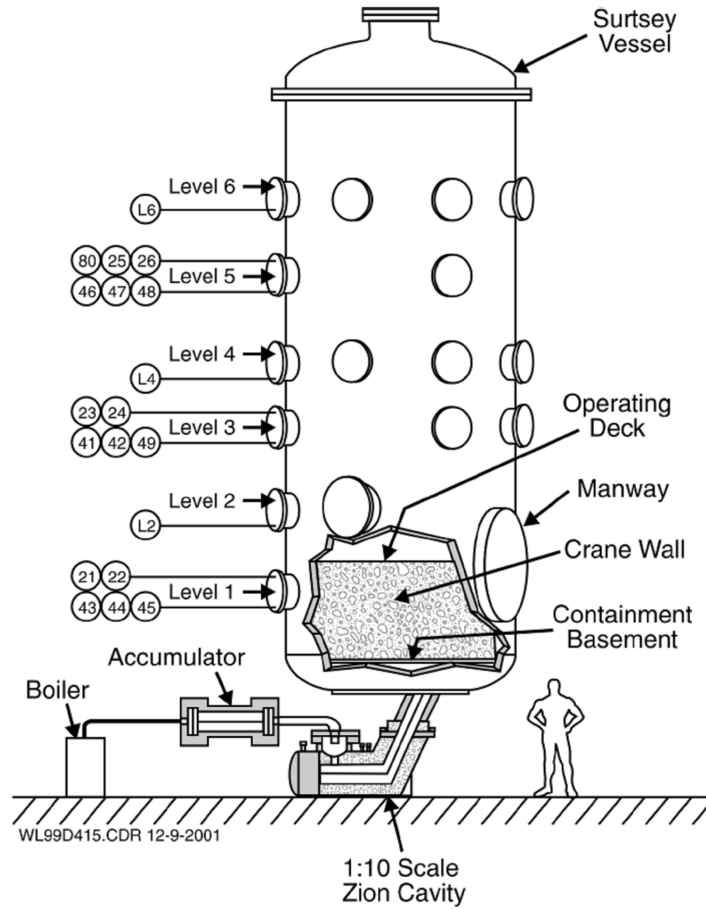


**Figure 21A-2. The IET Experiments Vessel, Ejection System, and Structures**  
 The Surtsey Vessel, High-Pressure Melt Ejection System, and Sub-Compartment Structures Used in the IET Experiments (Allen, et al., 1994).

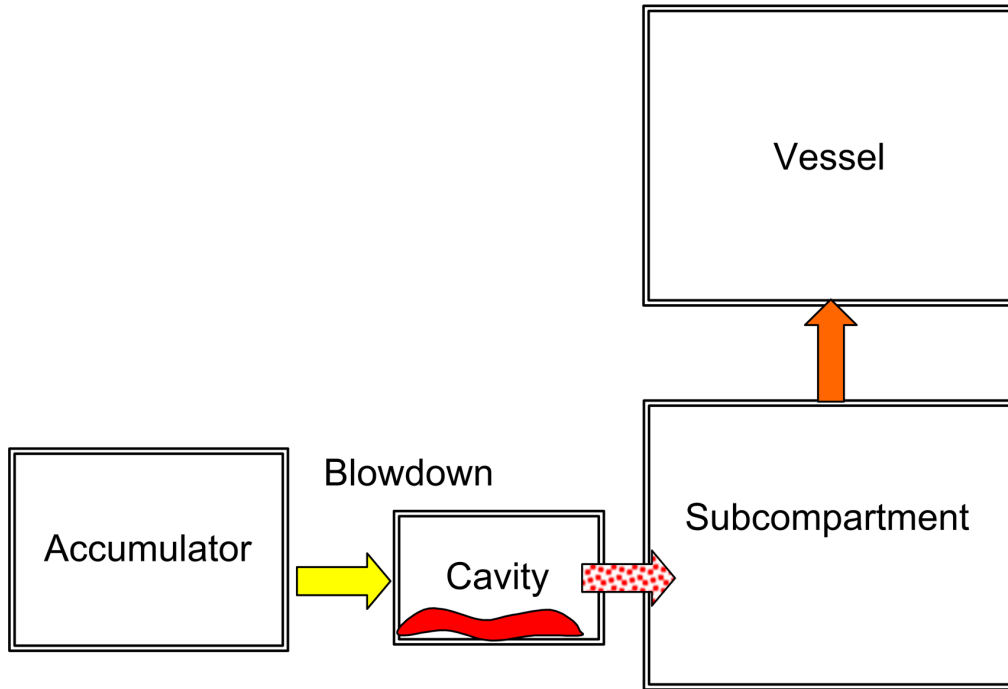


**Figure 21A-3. The IET Tests Transient CLCH Model Control Volumes Schematic**  
 Schematic of control volumes used in the implementation of the transient CLCH model to the interpretation of the IET tests.

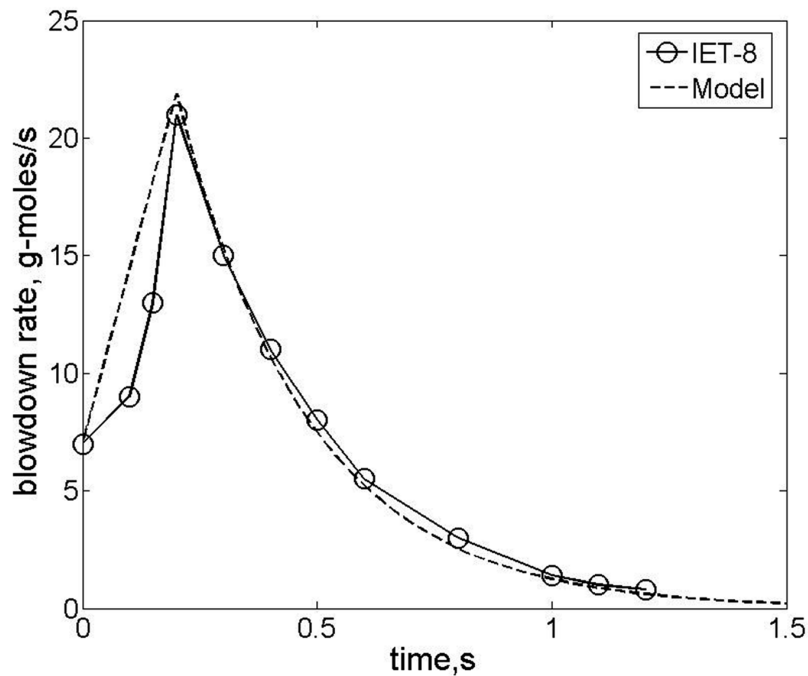


**Figure 21A-4. The blowdown rates for IET-8**

The blowdown rates measured in IET-8 and the approximate representation of the transition period utilized in the interpretation. The same was used for IET-1RR.

**Table 21A-1**  
**Parameters That Define the IET Tests Considered Here**

Parameters	Definitions	ANL	ANL	SNL
		IET-1RR	IET-8	IET-1
$V_{RCS}$ m <sup>3</sup> (ft <sup>3</sup> )	Volume of accumulator (simulating RCS)	0.0061 (0.22)	0.0061 (0.22)	0.345 (12.2)
$V_{subcomp}$ m <sup>3</sup> (ft <sup>3</sup> )	Freeboard volume inside subcompartment structures	0.072 (2.54)	0.072 (2.54)	4.64 (164)
$V_{dome}$ m <sup>3</sup> (ft <sup>3</sup> )	Volume of the dome (Simulating the containment)	1.51 (53.3)	1.51 (53.3)	85.15 (3007)
$D_{hole}$ ,cm (in)	Hole diameter	0.89 (0.35)	1.1 (0.43)	3.5 (1.4)
Initial containment gas conditions	% N <sub>2</sub>	99.90	37.4	99.90
	% O <sub>2</sub>	0.03	7.7	0.03
	% H <sub>2</sub>	0.00	3.9	0.00
	% H <sub>2</sub> O	0.00	50.0	0.00
	% CO <sub>2</sub>	0.01	0.0	0.01
	Other	0.06	0.0	0.06
$m_{corium}$ kg (lbm)	Mass	0.71 (1.6)	0.71 (1.6)	43 (95)
$T_{melt}$ ,K (°F)	Melt temperature	2550 (4130)	2550 (4130)	2550 (4130)
Melt composition	% Fe	52	52	52
	% Cr	11	11	11
	% Al	3	3	3
	% Al <sub>2</sub> O <sub>3</sub>	34	34	34
$P_{RCS}^0$ , MPa (psia)	Initial pressure of accumulator	6.7 (970)	6.5 (940)	7.1 (1000)
$T_{RCS}^0$ (K) (°F)	Initial temperature of accumulator	600 (620)	600 (620)	600 (620)

Table 21A-2

## Values of the Transient CLCH Model Parameters Used in the Interpretation

Parameters	Definitions	ANL	ANL	SNL
		IET-1RR	IET-8	IET-1
$\tau_{ejection}$ (s)	Ejection time during which steam and melt are ejected together	0.2	0.2	0.4
$\tau_m$ (s)	Entrainment time	0.24	0.24	0.74
$\Phi$	Oxidation efficiency	0.5	0.5	0.5

**Results for the ANL IET-8 and IET-1RR Tests**

The results are summarized in comparison to the experimental data in Figures 21A-5. We can see that both the pressurization rate and peak pressure reached are matched very well. The falloff of pressure at later times is due to heat losses, which are not represented in the model. There are 5.0 g (0.011 lbm) of hydrogen predicted to have been produced in comparison to the 4.8 g (0.0106 lbm) found in the experiment.

A parametric of the effect of the melt entrainment time on pressure, for a range around the predicted value of 0.24 s is shown in Figure 21A-5b. The effect on temperature is given in Figure 21A-5c. Consistently with the CLCH results presented originally, DCH loads increase as the DCH-scale (i.e. the melt entrainment time) increases—more of the stored steam is found in contact with the melt. Interestingly, in an open system such as the one of interest here, such an increase in DCH-scale would result in slower rates of pressurization, and thus lower peak pressures. The effect of the oxidation parameter ( $\Phi$ ) is examined in Figure 21A-5d. As expected the effect on pressure is minimal (one mole of steam produces one mole of hydrogen), and the small change seen is due to the different amounts of oxidation energy involved in each case.

The comparison to IET-1RR, as illustrated in Figure 21A-6 is very similar.

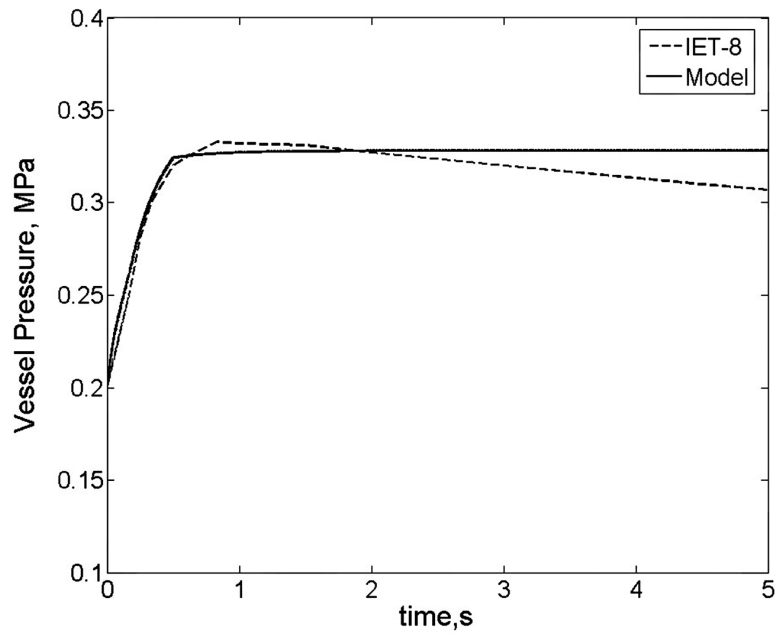


Figure 21A-5a. Pressure Transient Prediction and Measurement in Test IET-8

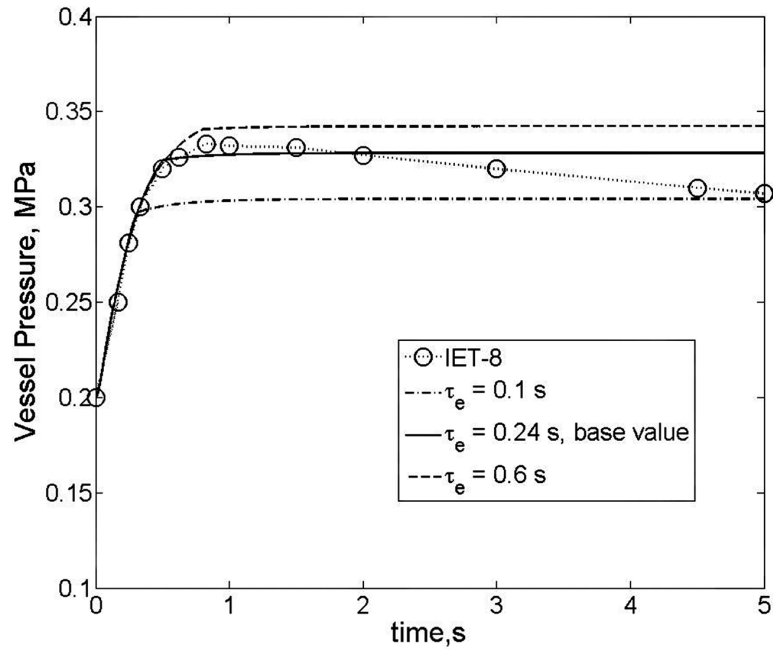


Figure 21A-5b. Sensitivity of Pressure Transient on Melt Entrainment Time

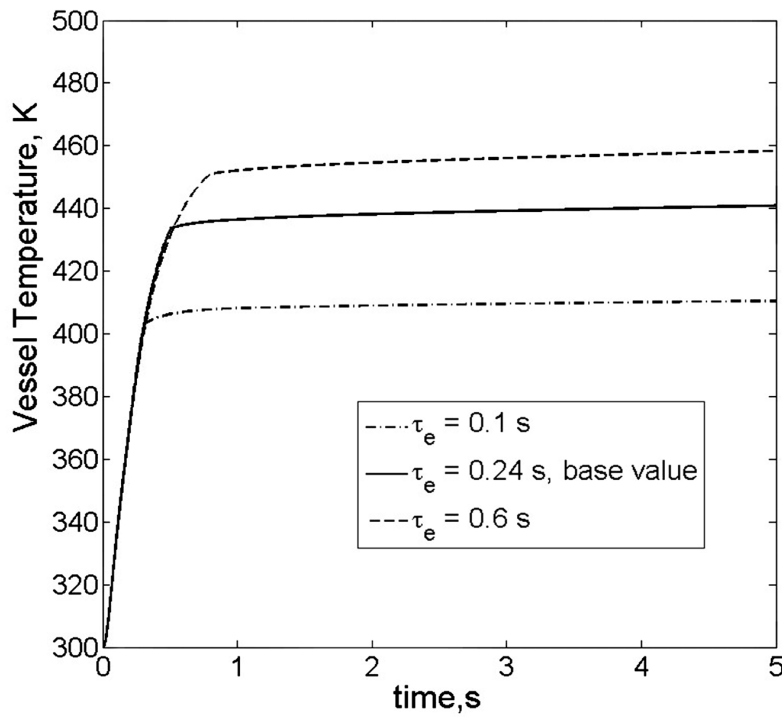


Figure 21A-5c. Sensitivity of Temperature Transient on Melt Entrainment Time



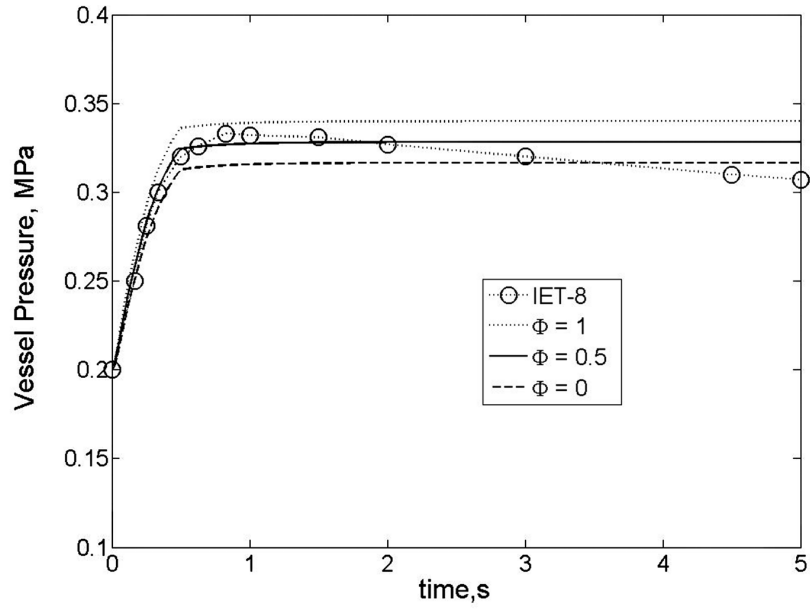


Figure 21A-5d. Sensitivity of Pressure Transient on the Oxidation Efficiency

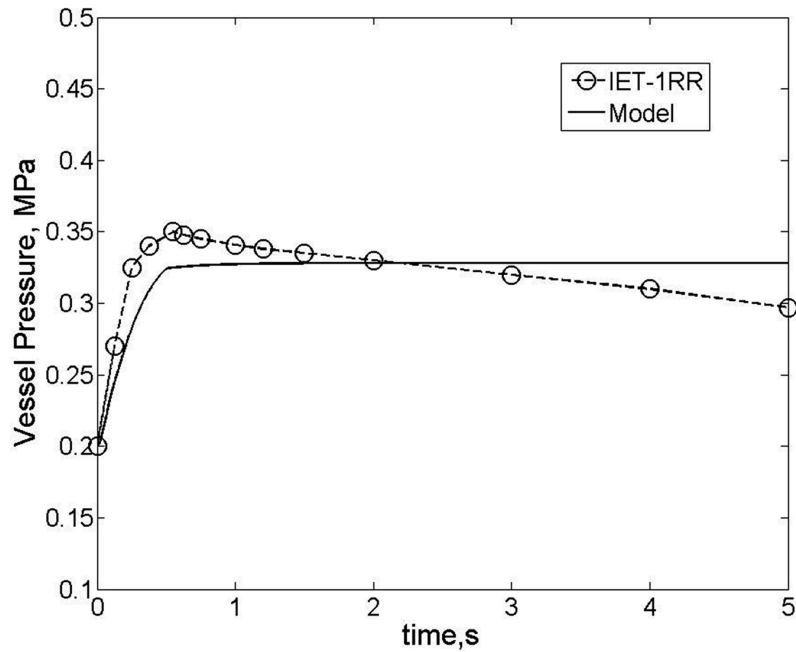


Figure 21A-6. Predicted and Measured Pressure Transients in Test IET-1RR

**Results for the SNL Test IET-1**

Measured and predicted pressure transients are shown in Figure 21A-7a. Note that due to the much smaller surface to volume ratio in this test, the rate of pressure loss (cooldown) is much less in comparison to the ANL tests, and the long-term agreement is better. A total of 174 g (0.384 lbm) of hydrogen produced in the calculation compare to 233 g (0.514 lbm) found in the experiment.

The temperature transients are compared in Figure 21A-7b. As shown by the data, temperatures depend on position in the short term. We note that around the time of 2 s, the elevation 1 and 3 data are quite close to the subcompartment temperatures calculated in the model, and that by 3 s all calculated and measured temperatures (with the exception of that at the highest point, elevation 5 converge to a close-together range. The later decay in the data is due to losses, which were not represented in the calculation.

A parametric on the melt entrainment time for a range around the predicted value of 0.74 s is shown in Figure 21A-7c. Again the larger the DCH-scale the higher the calculated loads, but note that this comes about through the turning over to an asymptote at different times, rather than through effecting the rate of pressure rise in the initial period.

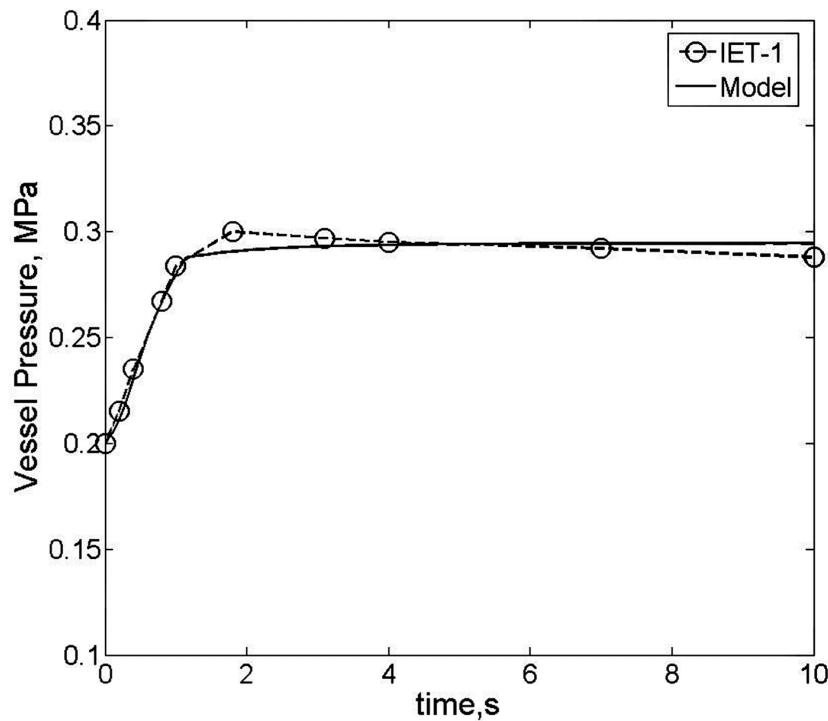


**Figure 21A-7a. Measured and Predicted Pressure Transients in Test IET-1**

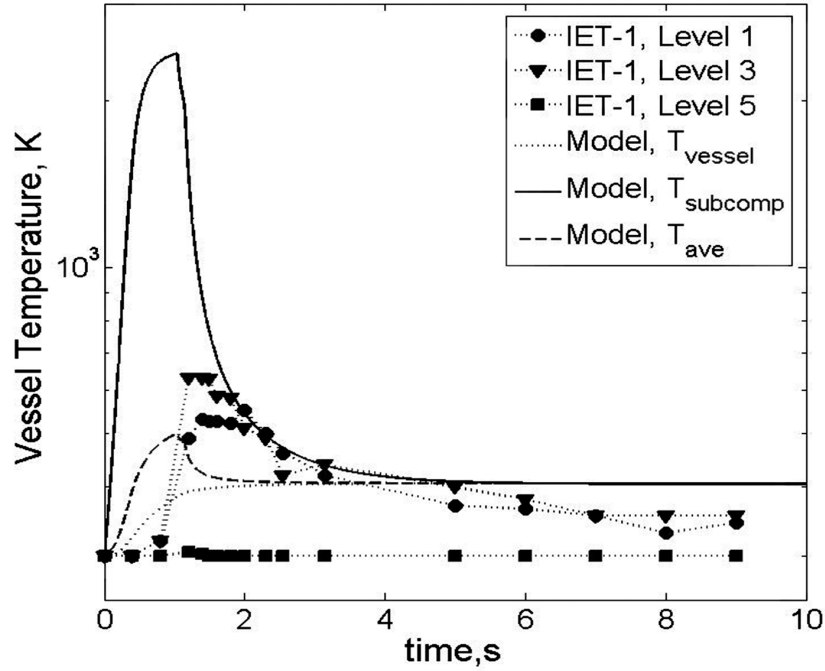


**Figure 21A-7b. Predicted and Measured Temperatures Transients in IET-1 Test**

Predicted and measured temperatures transients in IET-1 test. The positions to which the various levels refer to are shown in Figure 21A-2.

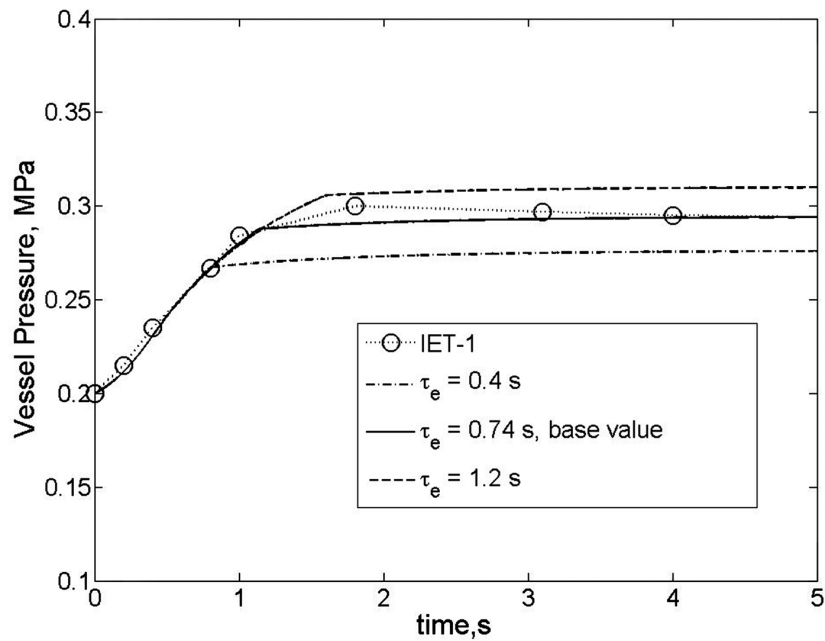


**Figure 21A-7c. Sensitivity of Pressure Transient on Melt Entrainment Time**

**21A.1 References**

- 21A-1 Allen, M. D., Pilch, M. M., Blanchat, T. K., Griffith, R. O., and Nichols, R. T. (1994), "Experiments to Investigate Direct Containment Heating Phenomena with Scaled Models of the Zion Nuclear Power Plant in the SURTSEY Test Facility," *NUREG/CR-6044, SAND93-1049*, Sandia National Laboratory, May 1994. Also, The Integral Effects Test (IET-1) in the Surtsey Test Facility. 1991 Water Reactor Safety meeting; 28-30 Oct 1991; Washington, DC (SAND-91-2613C).
- 21A-2 Binder, J. L., McUmbler, L. M., and Spencer, B. W. (1994), "Direct Containment Heating Integral Effects Tests at 1/40 Scale in Zion Nuclear Power Plant Geometry," *NUREG/CR-6168, ANL-94/18*, Argonne National Laboratory, September 1994.
- 21A-3 Pilch, M.M. Yan, H. and Theofanous, T.G. (1994), "The Probability of Containment Failure by Direct Containment Heating in Zion," *NUREG/CR-6075, SAND93-1535*, December 1994. M.M. Pilch, H. Yan and T.G. Theofanous, "The Probability of Containment Failure by Direct Containment Heating in Zion," *Nuclear Engineering & Design*, 164 (1996) 1–36.
- 21A-4 Yan, H. and Theofanous, T.G. (1993), "The Prediction of Direct Containment Heating," *ANS Proceedings 1993 National Heat Transfer Conference*, Atlanta, GA, Aug. 8-11, 1993, 294-309. Also H. Yan and T.G. Theofanous, "The Prediction of Direct Containment Heating," *Nuclear Engineering & Design*, 164 (1996) 95–116.

## 21B VALIDATION OF THE VENT-CLEARING MODEL FOR CLCH

### 21B.1 INTRODUCTION

In this Appendix we use data from the (Full-Scale) Pressure Suppression Test Facility (PSTF) tests (GE, 1974) to validate our model for vent clearing. A sensitive measure of this is the peak pressure obtained in the drywell during such an event. The PSTF tests were carried out in support of the Mark III pressure suppression containment concept using the horizontal vent system design as is the case for the ESBWR. More recently, PSTF tests were used for qualification of the TRACG code (GE, 1996) developed and used by GE for safety analyses of the GE ABWR, SBWR, and ESBWR designs under LOCA conditions (GE, 2003).

The facility consists of three major components as illustrated in Figure 21B.1-1. These components are (1) an electrically heated pressure vessel to represent the RPV, (2) another pressure vessel to represent the drywell volume, and (3) a suppression pool and wetwell volume. Steam blowdown was initiated by means of a rupture disc.

The horizontal vent system configuration of the ESBWR design is similar to the vent system configuration tested in the PSTF Test Series 5703. In both the PSTF and the ESBWR, the three horizontal vents are 0.70 m (28 in) in diameter, and they have a vertical spacing (center to center) of 1.37m (4.49 ft) (GE, 1974; GE, 2003). Also in both the PSTF and the ESBWR the total flow area of the horizontal vents is equal to the flow area of the vertical vent that leads to them. Other key geometric parameters in the experiments are summarized in Table B21.1-1. Two different break sizes were used: 63.5 mm (2.50 in) and 92.0 mm (3.62 in). Top-vent submergence values were varied between 2.06 m (6.76 ft) and 3.37 m (11.1 ft). The drywell was preheated to 93°C (200 °F) to minimize condensation effects. The main results are (i) vent clearing times and (ii) transient pressures in the drywell.

### 21B.2 MODEL FORMULATION

Figure 21B.2-1 illustrates the vent system in the PSTF (and the ESBWR). The system consists of a vertical pipe and three horizontal pipes. Increasing of drywell pressure due to blowdown leads to depression of the water level in the vertical vent pipe, and, subsequently to vent clearing, to flow of gases and steam to the suppression pool. The blowdown rate as measured in the tests is given in Figure 21B.2-2.

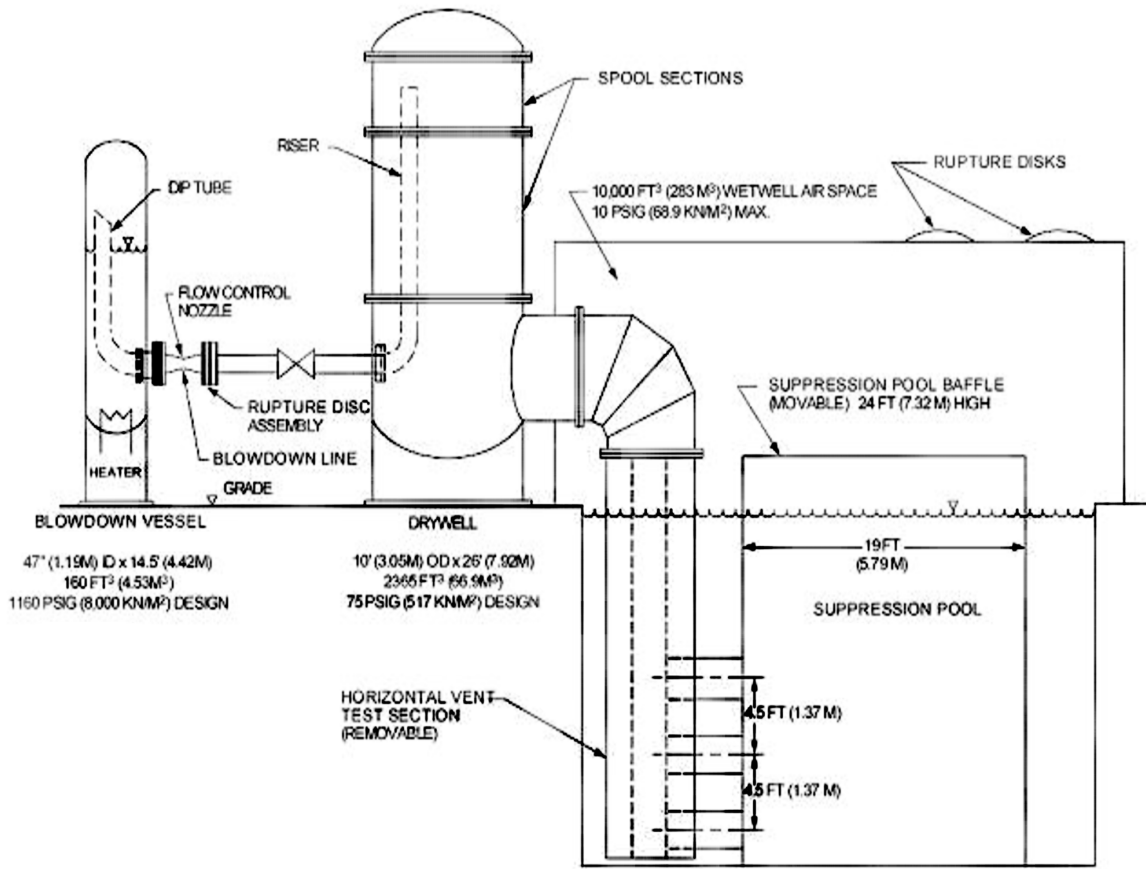
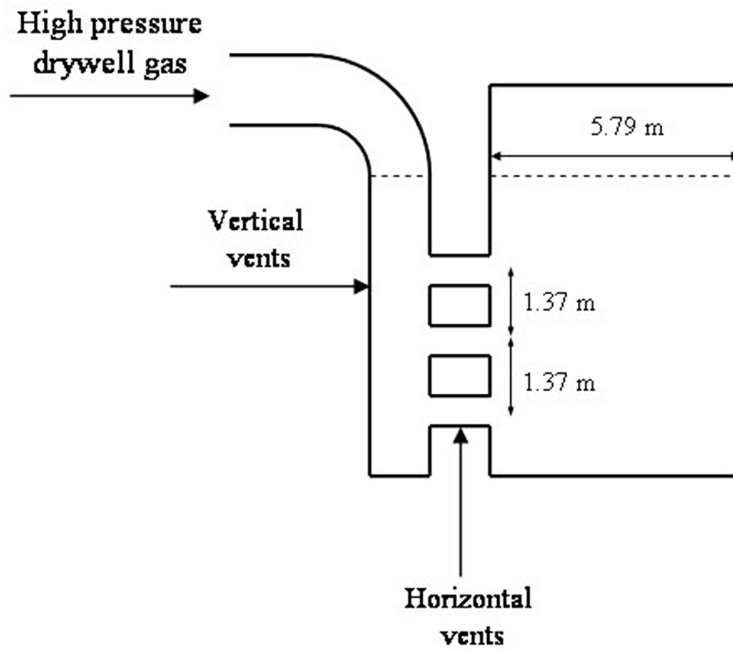


Figure 21B.1-1. Schematic of the PSTF (GE, 1974; GE, 2003)

**Table 21B.1-1**  
**Geometric Definition of the PSTF test series 5703**

Notation	Definitions	5703-1	5703-2	5703-3
	Number of horizontal vents	3	3	3
$D_{hole}$ mm (in)	Flow restrictor diameter	63.5 (2.50)	63.5 (2.50)	92.0 (3.62)
$H_{top,m}$ (ft)	Top vent submergence	2.06 (6.76)	3.33 (10.9)	3.37 (11.1)
$D_{vent}$ m (in)	Horizontal vent diameter	0.7 (28)	0.7 (28)	0.7 (28)
	Vertical axial spacing m (ft)			
	Top and Middle Vent	1.37 (4.49)	1.37 (4.49)	1.37 (4.49)
	Middle and Bottom Vent	1.37 (4.49)	1.37 (4.49)	1.37 (4.49)
$A_H$ m <sup>2</sup> (ft <sup>2</sup> )	Total area of horizontal vent	1.155 (12.43)	1.155 (12.43)	1.155 (12.43)
$A_v$ (m <sup>2</sup> )	Total area of vertical vent	1.131 (12.17)	1.131 (12.17)	1.131 (12.17)



**Figure 21B.2-1. The Vent Configuration in PSTF**

The Z coordinate origin is at the initial water level position and directed downwards.

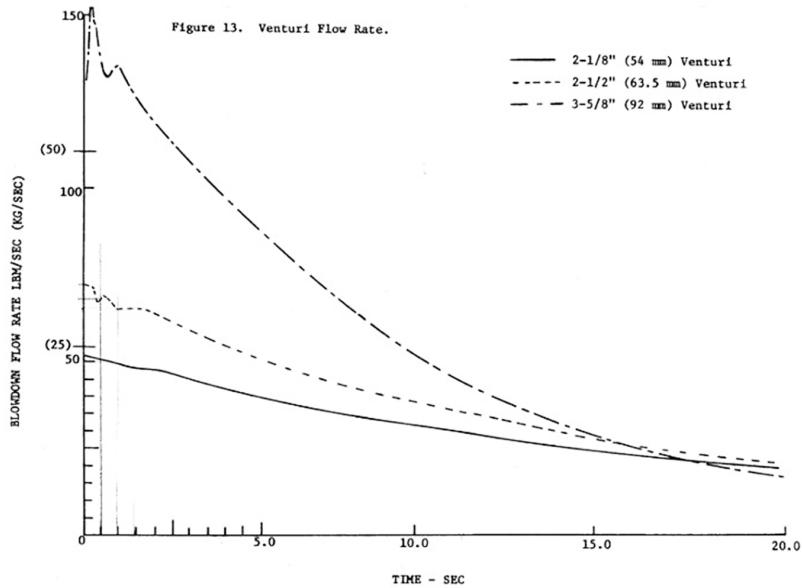


**Figure 21B.2-2. Blowdown Flow Rates Measured in Three PSTF Experiments (GE, 2003)**



The mechanical energy balance, written for a control volume that encloses all the liquid in both the vertical and horizontal vents is:

$$\frac{d}{dt} \left\{ \frac{1}{2} m_v u_v^2 + \frac{n}{2} m_h u_h^2 + \frac{n}{2} m_a u_h^2 + \frac{1}{2} m_v g (H - z) \right\} =$$

$$-\frac{n}{2} (\rho A_h u_h) u_h^2 - \rho g A_v u_v (H - \frac{1}{n} \sum_{i=1}^n Z_i) + P A_v u_v - \sum_{i=1}^n (P_0 + \rho g Z_i) A_h u_h - n \rho \frac{C_{d,junc}}{2} u_h^2 A_h u_h \quad (B21.1)$$

Where  $m$  is mass,  $u$  is velocity,  $A$  is flow area, subscripts  $v$  and  $h$  refer to vertical and horizontal vents respectively,  $P$  is pressure,  $\rho$  is density,  $g$  is acceleration of gravity,  $H$  is the initial water pool depth,  $Z_i$  is the submergence of vent  $i$  ( $i = 1, 2$  or  $3$ ).  $n$  is the total number of vents that are not cleared yet. The  $C_{d,junc}$  is a loss coefficient due to the 90° flow turn along with the flow area reduction by ~33%, which give a value of ~2. The masses in the vertical ( $m_v$ ) and horizontal vents ( $m_h$ ) and that due to the added mass ( $m_a$ ) can be written in terms of  $z$  the distance from the original position of the interface of the water slug,  $L$  the length of the horizontal vents, and  $D_h$  the diameter of the horizontal vents as:

$$m_v = \rho_L (H - z) A_v \quad m_h = \rho L A_h \quad m_a = \rho D_h A_h \quad (B21.2, B21.3, B21.4)$$

Then, using the fact that the flow area of the vertical vent is three times the flow area of each of the horizontal vents, and after some simplification we have:

$$\{(H - z) + L + D_h\} \frac{du}{dt} = \frac{P - P_0}{\rho} - gz - 2u^2 \quad \text{and} \quad u = \frac{dz}{dt} \quad (B21.5)$$

The general result, where  $n$  is the number of vents yet to be cleared, is:

$$\left\{ \frac{A_v}{n A_h} (L + D_h) + (H - z) \right\} \rho \frac{du}{dt} = P - (P_0 + \rho g z) - \frac{1}{2n^2} \left( \frac{A_v}{A_h} \right)^2 \rho u^2 (1 + C_{d,junc}) \quad (B21.6)$$

When the water level in the vertical vent reaches the elevation of a horizontal vent, the final stage to clearing can be described similarly by,

$$\frac{d}{dt} \left\{ \frac{1}{2} m_h u_h^2 + \frac{1}{2} m_a u_h^2 \right\} = -\frac{1}{2} (\rho A_h u_h) u_h^2 + P A_h u_h - (P_0 + \rho g Z_i) A_h u_h \quad (B.7)$$

or

$$(L + D_h) \rho \frac{du_h}{dt} = P - (P_0 + \rho g z) - \frac{1}{2} \rho u_h^2 \quad \text{and} \quad u_h = \frac{dx}{dt} \quad (B.8)$$

Where  $x$  is the length of the water slug in the horizontal vent.

Clearing of the horizontal vents is initiated if  $z = Z_h$ . After a horizontal vent is cleared (i.e.  $x > L$ ), the vapor flow through the vent is calculated based on standard equations for mass flow rate of ideal compressible gas through a tube, with an inlet pressure  $P$  (the pressure of the upper drywell) and an outlet pressure  $P_0 + \rho g Z_i$  (the hydrostatic pressure at the vent elevation). The loss of kinetic energy due to entrance, exit and friction is accounted by introducing the total loss coefficient  $K$ , which is the sum of losses due to flow entrance, turning, and exit, respectively. The actual vent rate  $G_{vent}$  is related to the ideal (no-loss) vent rate  $G_{vent,ideal}$  by  $G_{vent} = G_{vent,ideal}/(K+1)^{0.5}$ . The value of  $K$  used in these calculations was 3, and no attempt was made to fit the data by varying this or the other parameter in the model ( $C_{d,junc}$ ). The flow was checked for choking by the use of a critical pressure ratio of 2. At times that this condition was met the gas flow rate was set to that of ideal critical flow adjusted for losses by the same  $K$  factor.

### 21B.3 MODEL VALIDATION

As noted above the base values for the model parameters is  $C_{d,junc} = 2$  and  $K = 3$ . Calculations show that variations in the range  $1 < C_{d,junc} < 3$ , and  $1 < K < 6$  do not significantly influence the pressure transient. The results for the three tests considered are shown in Figures 21B.3-1 to 21B.3-3. Peak pressures and vent clearing times are summarized in Table 21B.3-1, along with the data, and the results of a previous benchmark exercise for the TRACG code (GE, 2003).

We can see first that the qualitative behavior of pressure rise and fall is predicted very well. Quantitatively the model slightly underestimates the rate of vent clearing and as a consequence overestimates the peak pressures reached by up to 12%, while the predictions remain consistently conservative for all three cases. Very likely this small error is due to gas breaking through the water slugs prior to complete vent clearing. The pressure oscillations that follow the main pressure event are of no interest here and their physics is not reflected in the formulation of the model.

**Table 21B-3**  
**Summary of Various Predictions Against the Experimental Data**

<b>Test Series</b>	<b>Description</b>	<b>Data</b>	<b>TRACG</b>	<b>Present</b>
5703-01	a. Short-term peak pressure, kPa (psia)	193 (28.0)	200 (29.0)	205 (29.7)
	b. Vent clearing time (s)			
	- Top vent	0.86	0.85	1.18
	- Middle vent	1.15	1.15	1.48
	- Bottom vent	DNC	DNC	DNC
5703-02	a. Short-term peak pressure, kPa (psia)	200 (29.0)	227.5 (33.0)	230 (33.4)
	b. Vent clearing time (s)			
	- Top vent	1.14	1.05	1.42
	- Middle vent	1.52	1.35	1.68
	- Bottom vent	DNC	DNC	DNC
5703-03	a. Short-term peak pressure, kPa (psia)	252 (36.5)	289.6 (42.0)	293 (42.5)
	b. Vent clearing time (s)			
	- Top vent	0.99	0.85	1.16
	- Middle vent	1.19	1.05	1.35
	- Bottom vent	1.60	1.30	1.93
Note: DNC denotes vent "do not clear".				

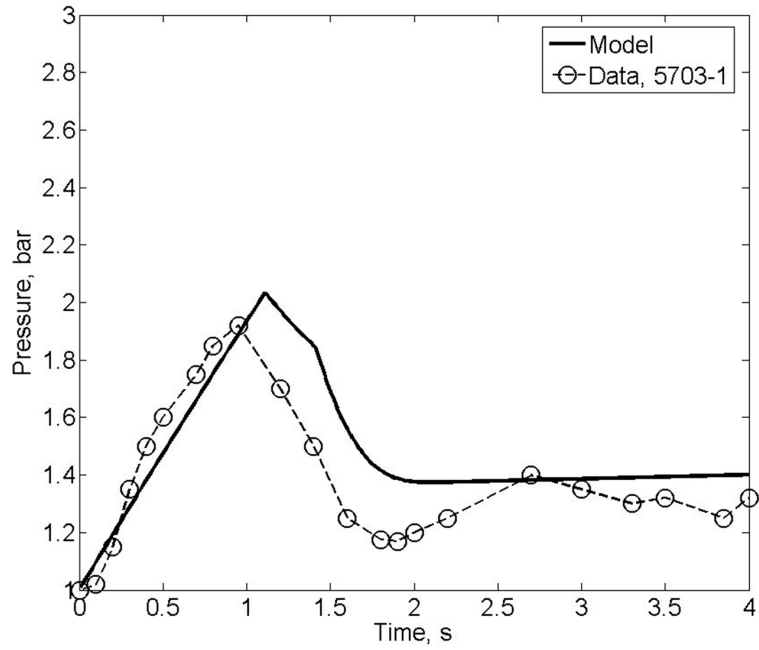


Figure 21B.3-1a Drywell Pressure Transient in Test 5703-1

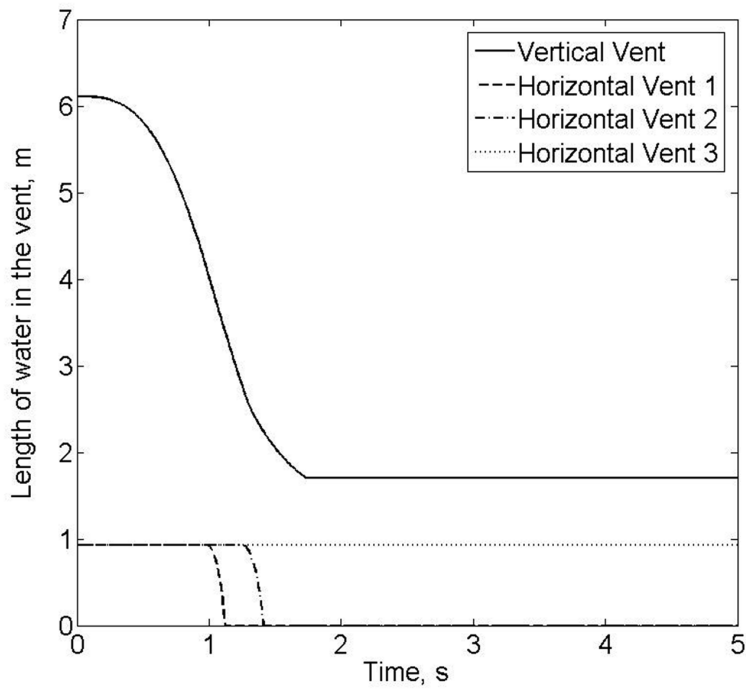


Figure 21B.3-1b. Predicted Dynamics of Vent Clearing in Test 5730-1  
The length is in meters

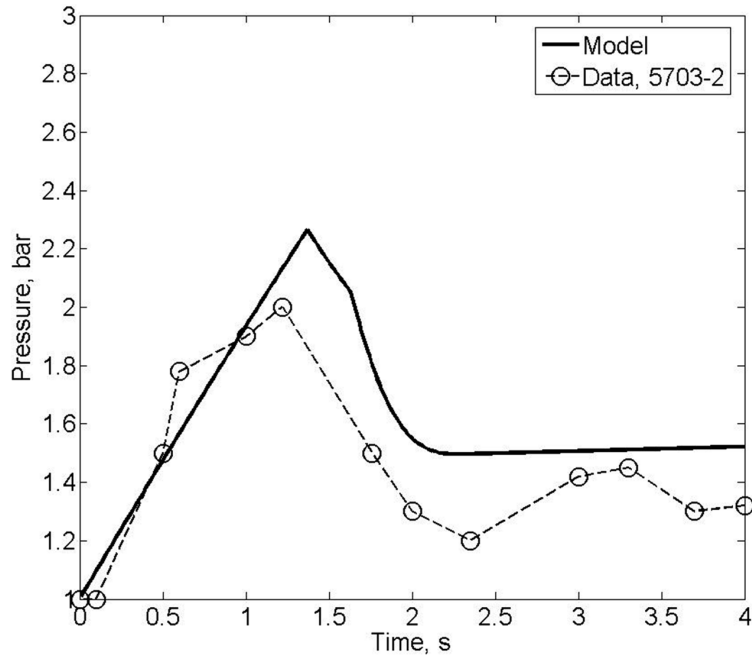


Figure 21B.3-2a. Drywell Pressure Transient in Test 5703-2

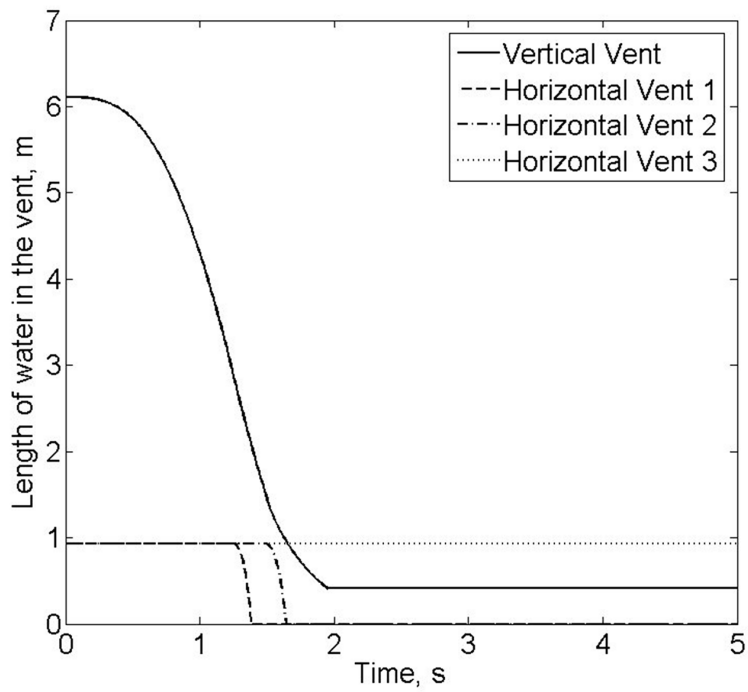


Figure 21B.3-2b. Predicted Dynamics of Vent Clearing in Test 5730-2

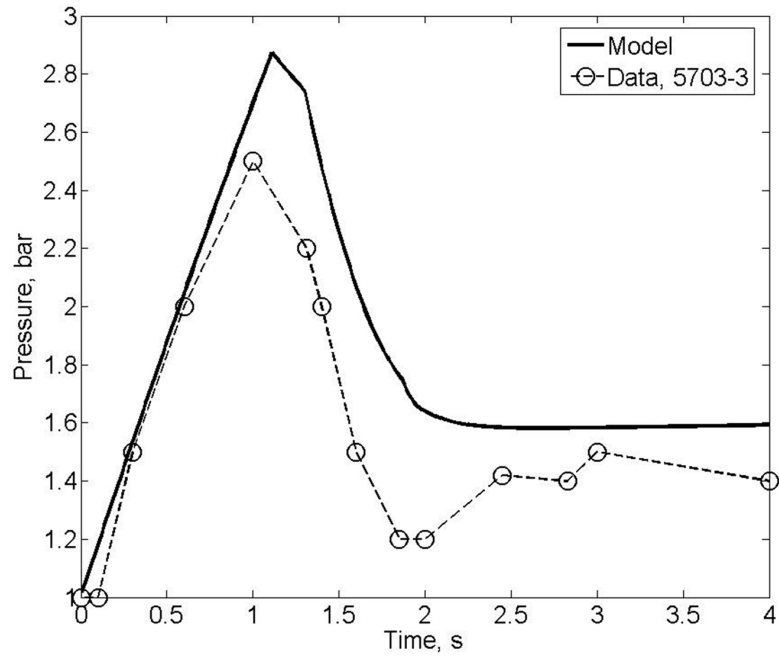


Figure 21B.3-3a. Dywell Pressure Transient in Test 5703-3

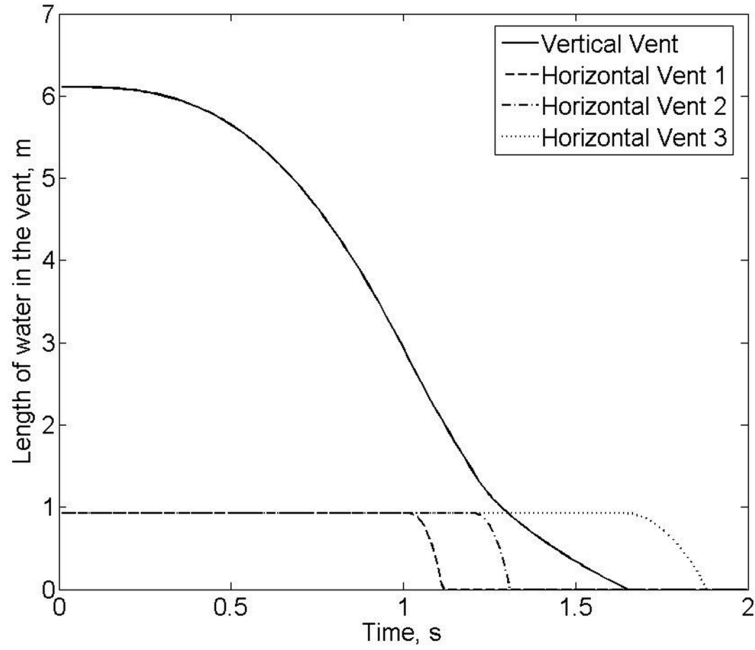


Figure 21B.3-3b. Predicted Dynamics of Vent Clearing in Test 5730-3

**21B.4 References**

- 21B-1 Batchelor G.K. (1967). An Introduction to Fluid Dynamics. Cambridge University Press.
- 21B-2 GE (1974). Mark III Confirmatory Test Program, Phase I - Large Scale Demonstration Tests, Test Series 5701 through 5703, NEDM-13377, October 1974.
- 21B-3 GE (1996). Licensing Topical Report, TRACG Model Description, NEDE-32176P, Revision 1, February 1996.
- 21B-4 GE (2003). J, R. Fitch et al., TRACG Qualification for SBWR. Vol.1 and 2. NEDO-32725P Revision 1. (2003).

## 21C VALIDATION OF THE CODES PM-ALPHA.L AND ESPROSE-M

### 21C.1 Validation Of The Codes Pm-Alpha.L And Esprose-M

As noted in the main body of the report these codes have been extensively verified and reviewed during the ROAAM resolution of in-vessel steam explosion for AP600 (Theofanous, 1999c). There is very little to add here, except perhaps that in the meanwhile we participated in the SERENA OECD-sponsored joint code exercise (SERENA, 2004, 2005). Thus we limit ourselves to a very high level overview, and some indicative results.

An overall perspective of the verification effort is provided in Figures 21C-1 and 21C-2. We can see that in both cases we paid attention to separate key aspects, such as the rapid momentum, heat and mass transport, including phase changes, in the plunging of hot particle clouds in water pool (i.e. Figure 21C-3) for PM-ALPHA, and the wave dynamics in multiphase media (i.e. Figure 21C-4) for ESPROSE.m. Note that special attention has been paid to the numerical aspects, as they impose rather severe challenges to stability and accuracy of such simulations. Also note the extensive use made of analytical solutions as they constitute absolute standards for testing the numerical results. Finally we note that these reports also contain comparisons (and discussions) with all available integral experimental data steam explosions (both premixing and propagation).



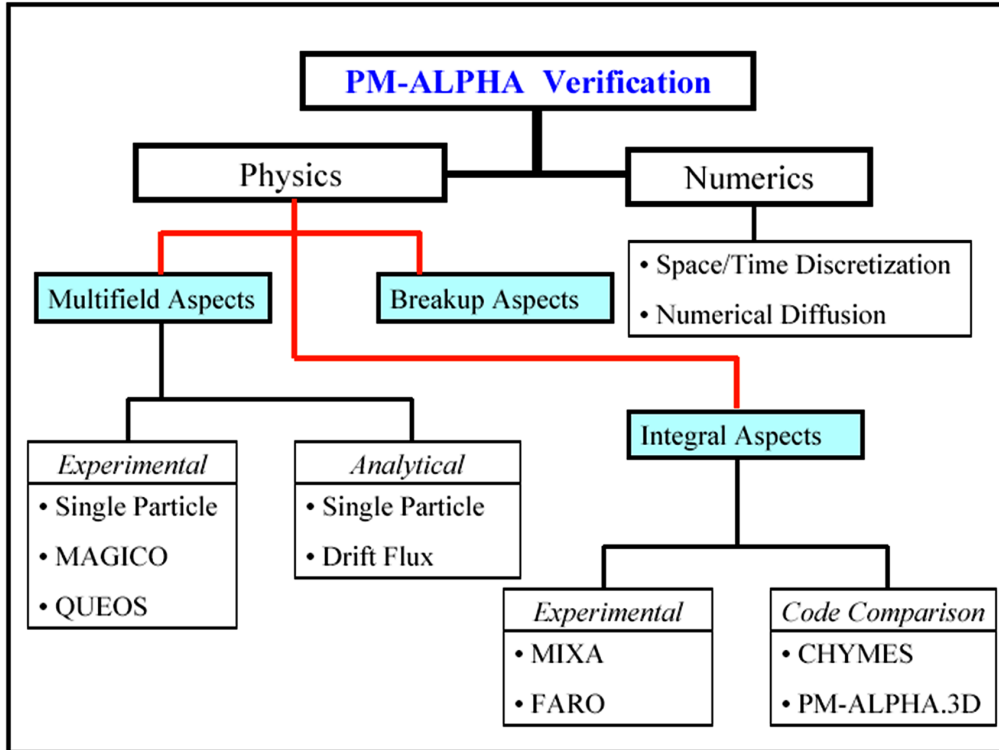


Figure 21C-1. Overview of the PM-ALPHA verification effort (Theofanous et al., 1999a)

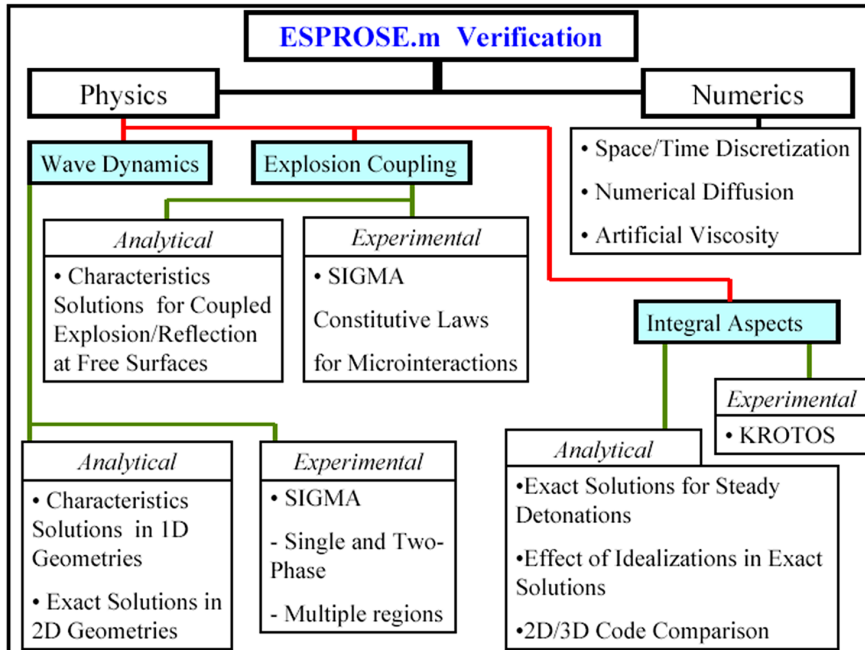
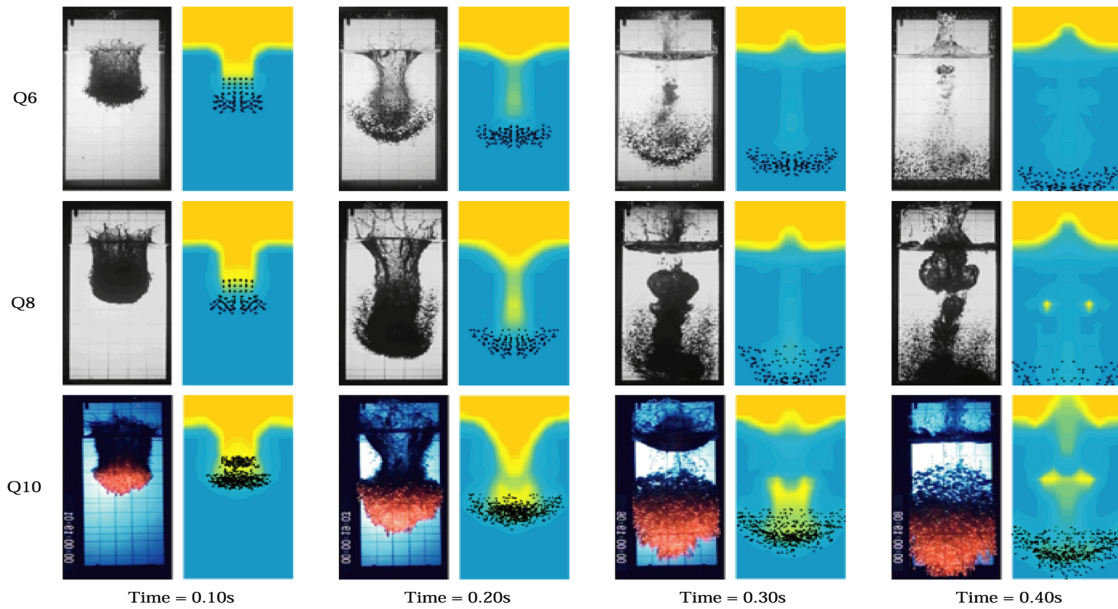
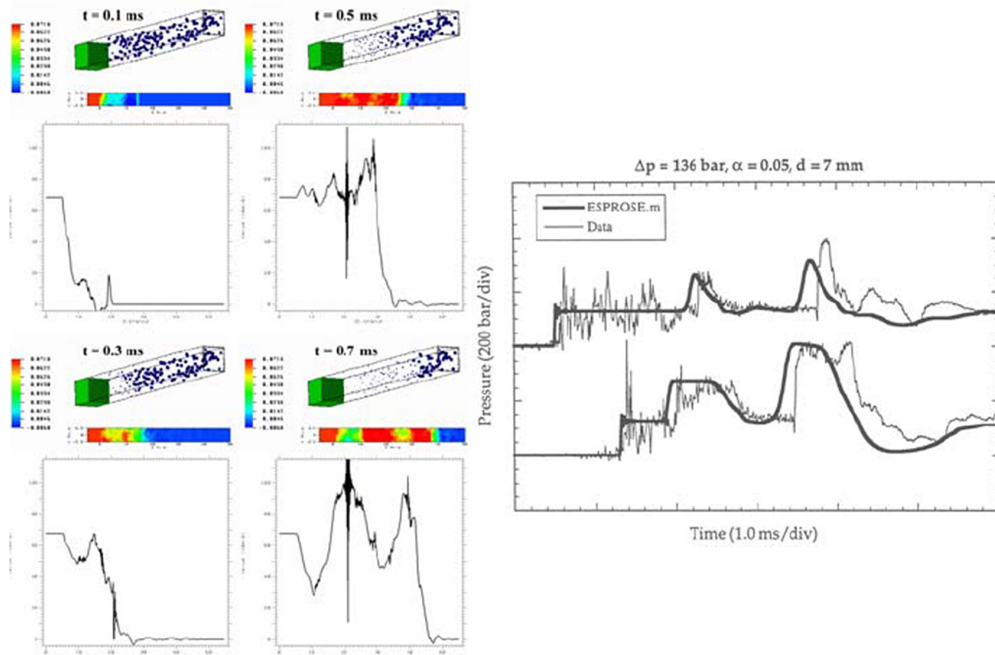


Figure 21C-2. Overview of the ESPROSE.m Verification Effort. (Theofanous et al., 1999b)



**Figure 21C-3. M-ALPHA Simulation of Particle Clouds Plunging into Water Pool**  
 PM-ALPHA simulation of particle clouds plunging into water pools (QUEOS experiments with different particle temperatures and coolant subcoolings). Note that the experimental images are in projection (external videos), while the simulations are shown in a vertical cross section.



**Figure 21C-4. Pressure Transient in a SIGMA Run and ESPOSE.m Simulation**  
 Right: Pressure transient measured in a multi-void-region SIGMA run and ESPOSE.m simulation. Left: DNS of this SIGMA run that captures also the pressure fluctuations due to collapsing bubbles.

**21C.2 REFERENCES**

- 21C-1 Theofanous, T.G. W.W. Yuen and S. Angelini (1999a), "The Verification Basis of the PM-ALPHA Code," *Nuclear Engineering & Design*, 189 (1999) 59-102. (Also T.G. Theofanous, W.W. Yuen and S. Angelini, "Premixing of Steam Explosions: PM-ALPHA Verification Studies," DOE/ID-10504, June 1998).
- 21C-2 Theofanous, T.G. W.W. Yuen, K. Freeman and X. Chen (1999b), "The Verification Basis of the ESPROSE.m Code," *Nuclear Engineering & Design*, 189 (1999) 103-138. (Also T.G. Theofanous, W.W. Yuen, K. Freeman and X. Chen, "Propagation of Steam Explosions: ESPROSE.m Verification Studies," DOE/ID-10503, June 1998).
- 21C-3 Theofanous, T.G. W.W. Yuen, S. Angelini, J.J. Sienicki, K. Freeman, X. Chen and T. Salmassi, (1999c) "Lower Head Integrity Under Steam Explosion Loads," *Nuclear Engineering & Design*, 189 (1999) 7-57. (Also T.G. Theofanous, W.W. Yuen, S. Angelini, J.J. Sienicki, K. Freeman, X. Chen and T. Salmassi, "Lower Head Integrity Under In-Vessel Steam Explosion Loads," DOE/ID-10541, June 1998).
- 21C-4 SERENA (2004) Identification of Relevant Conditions and Experiments for Fuel-Coolant Interactions in Nuclear Power Plants - SERENA Co-ordinated Programme Phase 1 Task 1 Final Report NEA/CSNI/R(2004)7. Also in D. Magallon1, K-H Bang, S. Basu, G. Berthoud, M. Bürger, M.L. Corradini, H. Jacobs, R. Meignen, O. Melikhov, K. Moriyama, M. Naitoh, J-H. Song, N. Suh, T.G. Theofanous, "Status of International Program SERENA on Fuel-Coolant Interactions," International Conference on Advances in Nuclear Power Plants (ICAPP-05) Seoul, May 15-19, 2005.
- 21C-5 SERENA (2005) Summary Record of the SERENA Task 4 Meeting. OECD/CSNI NEA/SEN/SIN/AMA(2005)13.

## 21D VALIDATION OF NATURAL CONVECTION MODEL FOR CORIUM MELTS

### 21D.1 VALIDATION OF NATURAL CONVECTION MODEL FOR CORIUM MELTS

The purpose of this Appendix is to summarize evidence that our Computation Fluid Dynamics (CFD) simulations of natural convection in volumetrically heated pools, as carried out for purposes of this effort, are the culmination of long experience with this type of work both at the experimental as well as the computational fronts: Theofanous et al. (1996), Dinh and Nourgaliev (1997), Dinh et al. (1997) and Theofanous and Angelini (2000).

The issues of particular concern here are (a) the up-to-downward power split, and (b) the heat flux distribution along the inclined boundaries of a volumetrically heated pool that is of the shape of a wedge. The conditions are turbulent convection, a regime characterized by very high values of the Rayleigh number, and a regime that has been difficult to approach in the past, both experimentally and computationally. The computational issues are those of grid resolution, as needed for keeping numerical diffusion from contaminating the actual transport involved. As a result computations are becoming more and more demanding as the Rayleigh numbers get bigger and bigger. The experimental issues had to do with achieving uniform volumetric heating in a large geometry, so as to match prototypic Rayleigh numbers of interest to reactor applications. The experimental problem was resolved by the ACOPO concept (Theofanous and Angelini, 2000), who also established the correspondence between the “external” (externally heated/cooled system) and the “internal” (volumetrically heated, externally cooled system) problems, and produced unified correlations valid up to the range of interest to whole-core reactor melt pools.

The computational issues turn out to be more insidious (Dinh and Nourgaliev, 1997), but eventually a reasonable understanding emerged, as verified by comparison to experiments (Dinh et al, 1997; Nourgaliev and Dinh, 1997). Heat transfer from the pool is driven by (a) fluid’s unstable stratification, which induces intense mixing in the bulk and near the upper cooled boundary, and (b), organized fluid motions, and “cold” boundary layers descending along the side and inclined lower boundaries.

In particular, we showed that mixing anisotropy is central to the understanding and modeling (Reynolds-type model) of high Rayleigh-number thermal convection of the type that is of primary interest in reactor applications. Further, analyses using a “no-model” (meaning no subgrid scale model) Large Eddy Simulation (LES) showed that, given sufficient resolution, the method works quite well in predicting mixing and heat transfer in volumetrically heated liquid pools, and for pools, such as the ACOPO experiment, that approximate this condition by being subjected to externally-imposed transient cool-down (Nourgaliev et al. 1997a, 1997b and Figures 21D-1 and 21D-2).

It was also established that 2D simulations of thermal convection in volumetrically heated liquid pools are capable of capturing reasonably well the  $Nu = f(Ra)$  dependence, although at the very high Rayleigh-number range ( $Ra_E \sim 10^{12}$ ) the absolute values were somewhat lower than those measured in experiments. On the other hand, 3D simulations, which adequately capture all degrees of freedom, were found to improve both numerical convergence and energy balance. Based on our previous works, we favor the QUICK-modified, third-order bounded CCCT upwinded scheme (Nourgaliev and Dinh, 1997).

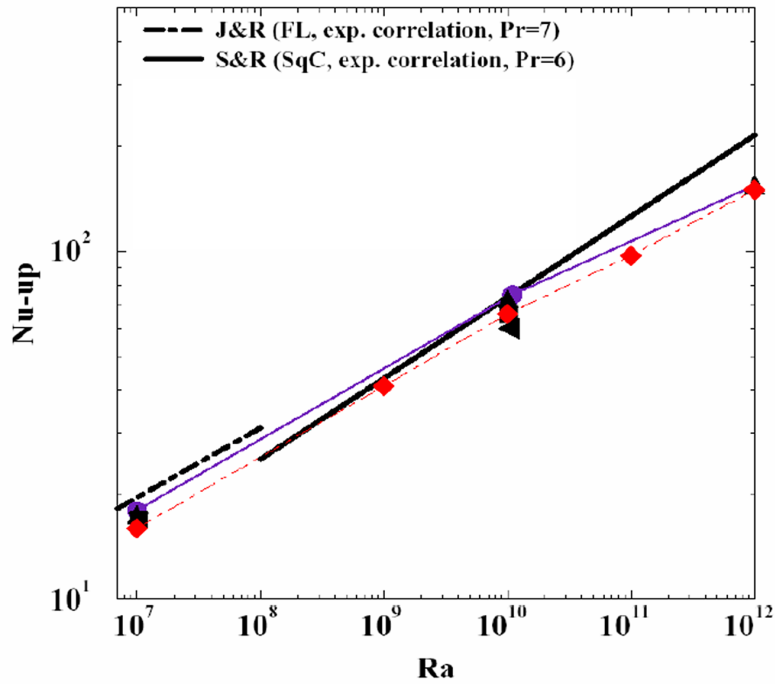


**Figure 21D-1. Upward Nusselt Number From an Internally Heated Fluid Layer**

The numerical simulations utilize the no-model LES and the QUICK scheme. • – simulation for  $Pr = 7$ ; ♦ – simulation for  $Pr = 0.45$ ; ◀ – simulation for  $Pr = 0.2$ . As the Ra increases to the range of  $10^{12}$ , the upward heat fluxes predicted by 2D simulations tend to be somewhat lower than experimental correlations (Steinberner and Reineke, 1978, Jahn and Reineke, 1974).

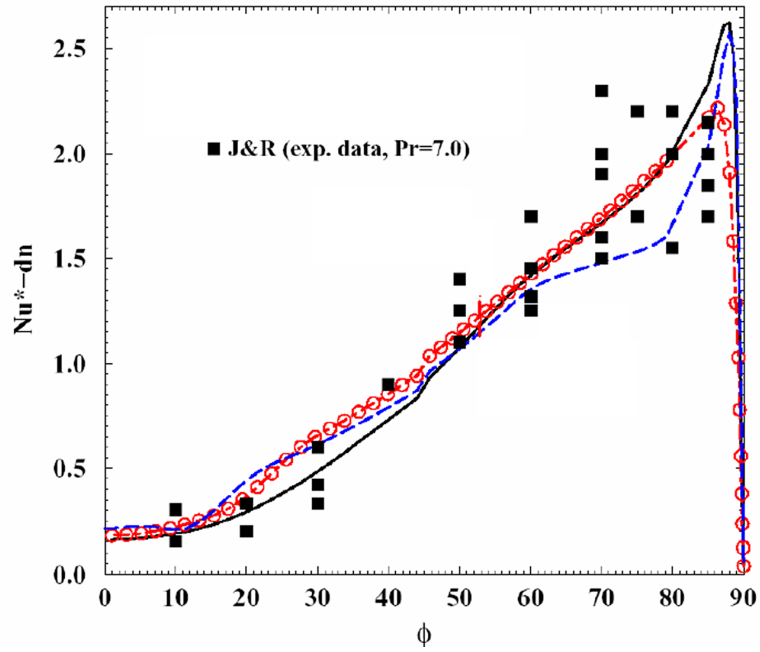


**Figure 21D-2. Simulation of Heat Flux Distribution in a Liquid Pool**

Simulation of heat flux distribution (relative to the area-averaged value) on the downward surface in a volumetrically heated semicircular liquid pool (Jahn and Reineke data, 1974). (Solid black line, red circles, and dotted blue line are simulations for Pr =7; 1.2; 0.6, respectively).

More recently we have used the Fluent CFD code as a platform to further pursue these numerical issues in the scope of a new, unique, and highly sensitive experiment conducted in our laboratory at UCSB.

Named the BETA-NC experiment, the experimental approach stems from our work developed under a NASA grant to investigate pool boiling (Figure 21D-3). The objective is to gain insights into the physics of unstably stratified layers, and in particular to obtain transient data which characterize the emergence of flow structures. This kind of experiment and the approach are unique to enabling an a priori testing of fidelity of this type of (instability/self-organization) phenomena.

Uniform heat flux on the BETA heated surface is achieved by passing a direct electrical current through a 460nm-thin Titanium film, vapor-deposited on 130  $\mu\text{m}$  borosilicate glass substrate. The Titanium film is highly uniform in thickness, and so is the surface heat flux due to Joule heating. Also, because of the small thickness of the Titanium film and the glass substrate, temperature response and measurement are on a millisecond time scale, which is much shorter than the time scale of the convection process (it occurs on a time scale of seconds). The test section used is a rectangular glass vessel, closed at the bottom by the heater element, it occupying the entire 27x40  $\text{mm}^2$  cross section of the vessel. We use an infrared camera to achieve a high-speed (1 KHz), high-resolution (30  $\mu\text{m}$ ), highly accurate ( $\pm 0.3\text{K}$ ) thermometry of the heater surface (Dinh et al., 2004a, 2004b).

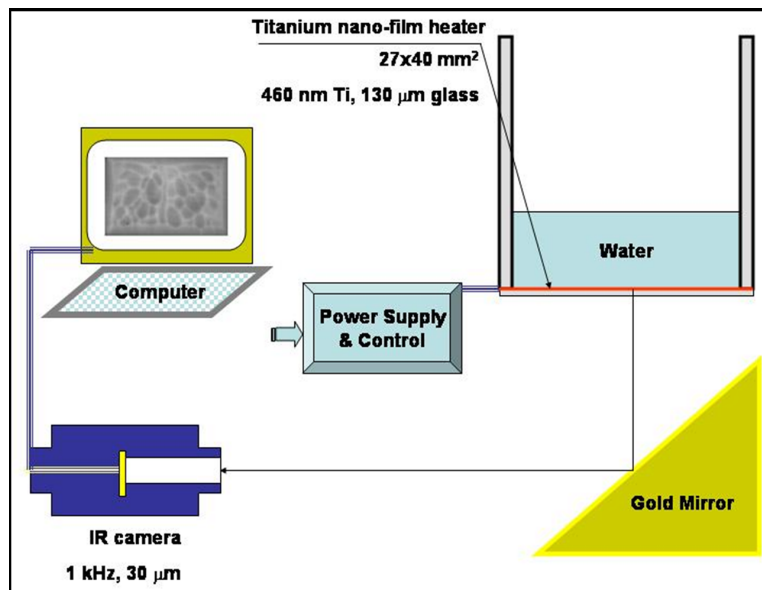
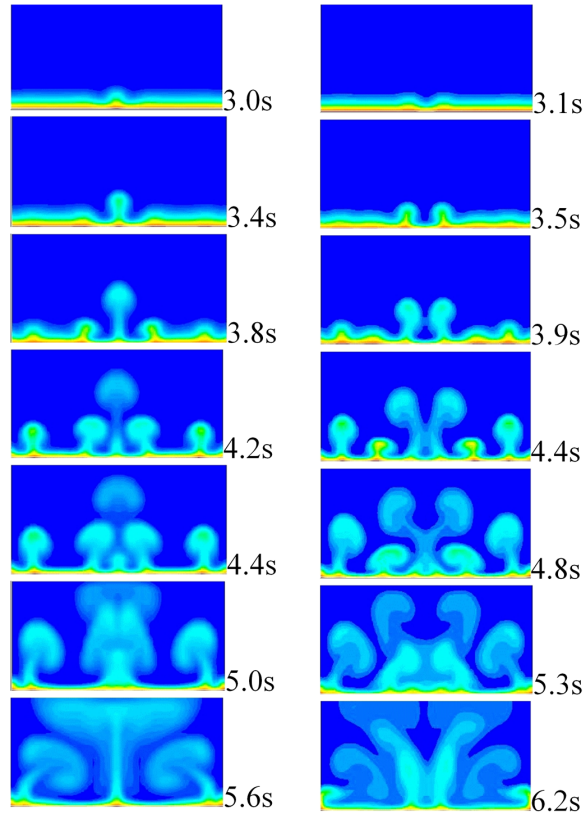
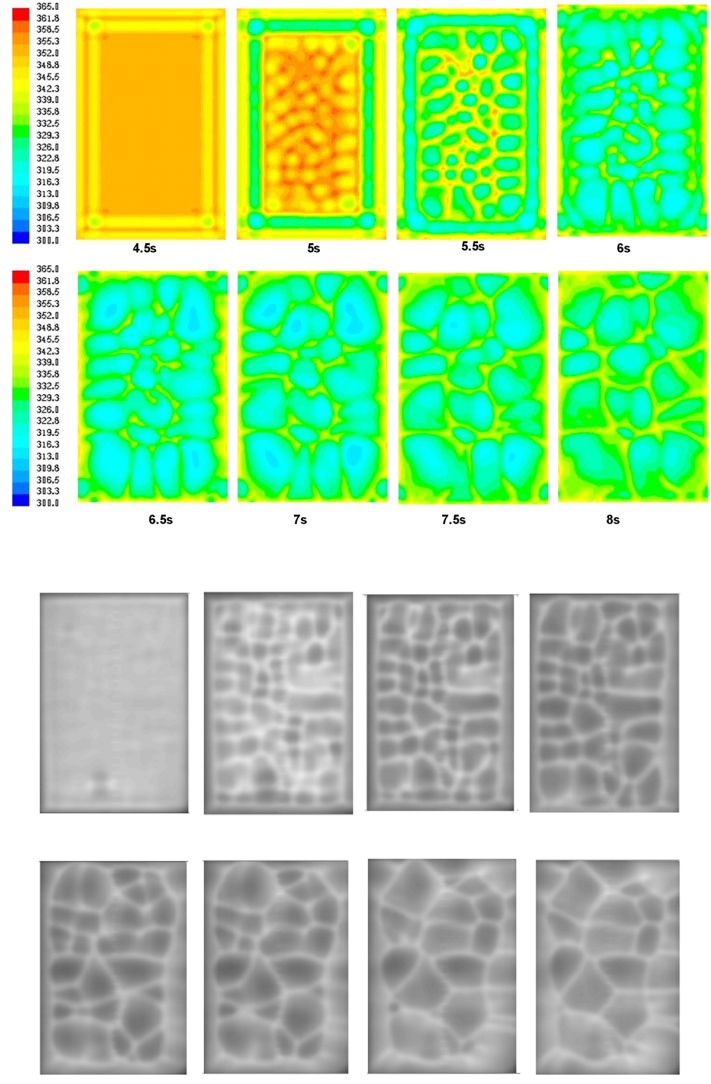


Figure 21D-3. BETA-NC experiment for the study of thermal convection



**Figure 21D-4a. Numerical simulation of fluid instability, and Rayleigh-Bernard convection in fluid layer heated from below**





**Figure 21D-4b. Transient thermal convection patterns emergent upon heating, as visualized by temperature maps of the heating surface**

Top: Surface temperature of a fluid layer as obtained from our numerical simulations. Bottom: Heater surface temperature as measured by a high-speed IR camera in a BETA-NC experiment (Dinh et al., 2004a). Both inception of instability and thermal patterns can be reproduced in this basic-principles simulation.

For these BETA-NC simulations, we examined first-order (SIMPLE), second-order (SIMPLEC, QUICK) accurate numerical schemes, and tested the effect of parameters of spatial and time discretization. Figures 21D-4 provide a sample set of simulation results.

In Section 21.5 (BMP) heat transfer results obtained from natural convection simulation for BiMAC melt pool configurations were presented and used for the thermal load assessment. Additional perspectives on these numerical simulations are provided in Figures 21D-5 and 21D-6 addressing aspects of temporal and spatial resolution.

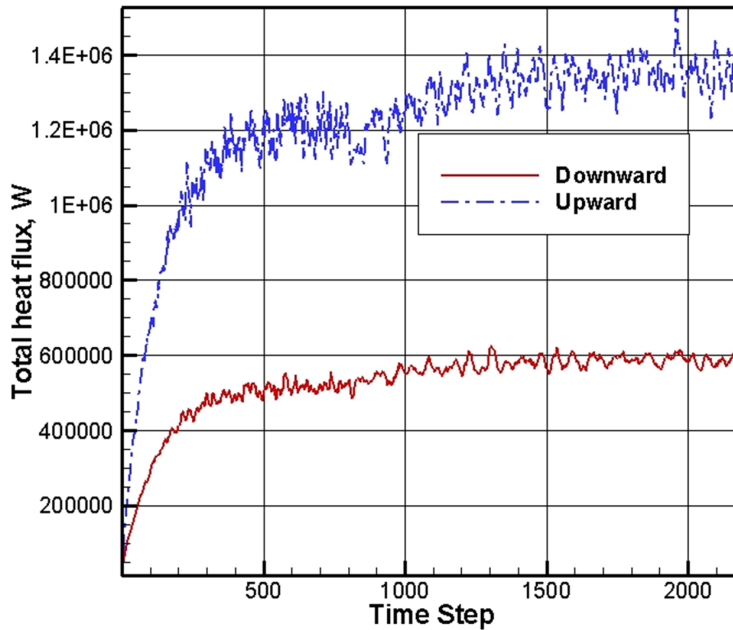


**Figure 21D-5. Heat Removal Rates of a Volumetrically Heated Liquid Pool**

Heat removal rates to top and bottom boundaries of a volumetrically heated liquid pool (Configuration C 2D simulation). During the first 800 time steps, the simulation was performed with a coarse time step, to establish the overall flow pattern, after which the time step was reduced by about an order of magnitude, to ensure adequate resolution of flow mixing in the unstably stratified region (top boundary). The refinement lead to an increase of both heat fluxes by ~ 20%, so the energy split remained the same.

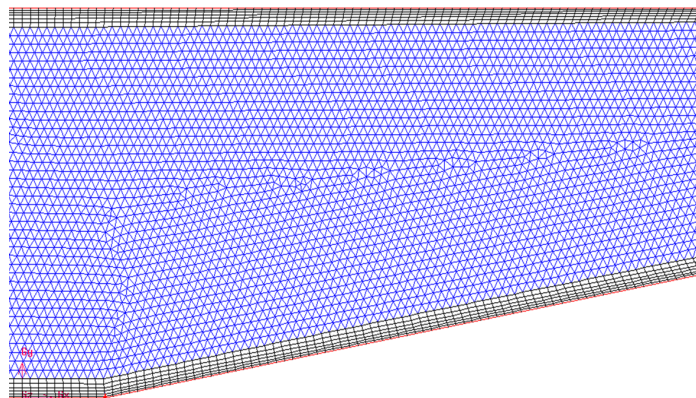


**Figure 21D-6. Grid with refinement in the near-wall region**

Grid with refinement in the near-wall region. Sensitivity calculations were run on different grids to ensure that we achieved convergence.

**21D.2 REFERENCES**

- 21D-1 Dinh T.N. and R. R. Nourgaliev, "Turbulence Modeling in Large Volumetrically Heated Liquid Pools," *Nuclear Engineering and Design*, 169 131-150 (1997).
- 21D-2 Dinh, T.N. R.R. Nourgaliev, and B.R. Sehgal, "On Heat Transfer Characteristics of Real and Simulant Melt Pool Experiments," *Nuclear Engineering and Design*, 169, pp.151-164, 1997.
- 21D-3 Dinh, T.N. Y.Z. Yang, J.P. Tu, R.R. Nourgaliev and T.G. Theofanous (2004a), "Rayleigh-Bénard Natural Convection Heat Transfer: Pattern Formation, Complexity and Predictability," 2004 International Congress on Advances in Nuclear Power Plants, Pittsburgh, PA, June 13-17, 2004.
- 21D-4 Dinh, T.N. J.P. Tu, Y.Z. Yang, R.R. Nourgaliev and T.G. Theofanous (2004b), "Characterization and Predictability of Transient Heat Transfer in an Unstably Stratified Layer during Power Startup," 37th AIAA Thermophysics Conference, Portland, OR, June 27-30, 2004. AIAA-2004-2733.
- 21D-5 Grenoble: (1994). OECD/CSNI/NEA Workshop on Large Molten Pool Heat Transfer, Nuclear Research Centre, Grenoble, France, March 9-11.
- 21D-6 FLUENT CFD Code. User Manual. 2003.
- 21D-7 FLUENT 6.0 Validation Experience and Applications. Fluent and Fluent users websites.
- 21D-8 Jahn M. and H.H. Reineke (1974), "Free Convection Heat Transfer with Internal Heat Sources: Calculations and Measurements," Proceedings of the 5th Int. Heat Transfer Conference, Tokyo, Japan, Vol. 3, paper NC.2.8.
- 21D-9 Nourgaliev, R.R. and T.N. Dinh, "The Investigation of Turbulence Characteristics in an Internally Heated Unstably Stratified Fluid Layers," *Nuclear Engineering and Design*, 178:(1), 235-259 (1997).
- 21D-10 Nourgaliev, R.R. T.N. Dinh, and B.R. Sehgal, "Simulation and Analysis of Transient Cooldown Natural Convection Experiments," *International Journal of Nuclear Engineering and Design*, 178:(1), pp.13-27 (1997a).
- 21D-11 Nourgaliev, R.R. T.N. Dinh, and B.R. Sehgal, "Effect of Fluid Prandtl Number on Heat Transfer Characteristics in Internally Heated Liquid Pools with Rayleigh Numbers up to  $10^{12}$ ," *Nuclear Engineering and Design* 169 165-184 (1997b).
- 21D-12 Steinberner U. and H.H. Reineke (1978), "Turbulent Buoyancy Convection Heat Transfer with Internal Heat Sources," Proceedings of the 6th Int. Heat Transfer Conference, Toronto, Canada, Vol.2, pp.305-310.
- 21D-13 Theofanous, T. G., C. Liu, S. Additon, S. Angelini, O. Kymäläinen, and T. Salmassi, In-Vessel Coolability and Retention of a Core Melt, DOE/ID-10460, October 1996.
- 21D-14 Theofanous, T. G. and S. Angelini, "Natural Convection for In-Vessel Retention at Prototypic Rayleigh Numbers," *Nuclear Engineering and Design* 200 1-9 (2000).

## 21E VALIDATION OF 2-PHASE NATURAL CIRCULATION MODEL IN BIMAC

### 21E.1 INTRODUCTION

In this Appendix we examine aspects of two-phase natural circulation in BiMAC, as assessed by means of a model developed specifically for this work. The Model is described in Section 21E.2. A validation exercise using the pressure drop data from the SULTAN experiment is presented in Section 21E.3. Application to BiMAC is then given in Section 21E.4. Our principal interest is two-phase pressure drop in heated, low-inclination channels of a flow cross-section that is of the order of ~0.10 m (3.9 in) (large in comparison to most past experiments in this area).

### 21E.2 THE TWO-PHASE FLOW MODEL

The governing equations for homogeneous two-phase flow in the 1D equilibrium approximation, are summarized in Table 21E.2.1 — the nomenclature can be found at the end of this appendix. The vapor quality  $x$  is the local equilibrium value according to energy conservation. The total pressure drop is obtained by integrating along the flow path ( $dl$ ) the differential pressure gradients due to gravity, acceleration, and viscous losses, i.e.,

$$\frac{dp}{dl} = \frac{dp_b}{dl} + \frac{dp_f}{dl} + \frac{dp_a}{dl} \quad (\text{E.21.1})$$

The local void fractions, and two-phase viscous losses are from the Lockhart-Martinelli (1949) correlation applied in a quasi-steady fashion (see Wallis, 1969 as a more convenient reference). As second approach, we also make use of arbitrary specification of uniformly applied values of vapor slip, and using it, we obtain the local void fractions through the local quality. The correction for inclination (E.21.3) is similar to a generalization from data obtained on inclined pipes by Snerova et al (1961).

Table 21E.2-1.

Definition of the Two-Phase Flow Model

Energy balance:

$$G \frac{d(xA)}{dl} = \frac{qU}{H_{fg}}$$

Void Fraction and Density

$$\beta = \frac{x}{x + \frac{(1-x)\rho_v}{\rho_w}}$$

$$\alpha_v = \frac{\beta}{\beta + s(1-\beta)}$$

$$\alpha_v = (1 + X_{tt} + 1/F_t)^{-0.321} \tag{E.21.2}$$

where  $X_{tt} = \left(\frac{1-x}{x}\right)^{0.9} \left(\frac{\rho_v}{\rho_w}\right)^{0.5} \left(\frac{\mu_w}{\mu_v}\right)^{0.1}$

and  $F_t = \left(\frac{x^3 G^2}{\rho_v^2 d g (1-x)}\right)^{0.5}$

$$\alpha = \begin{cases} \alpha_v & \text{if } \theta = \pi/2 \\ \xi \cdot \alpha_v & \text{if } \theta < \pi/2 \end{cases} \tag{E.21.3}$$

where  $\xi = \frac{\beta + s \cdot (1-\beta)}{\beta + Y \cdot s(1-\beta)}$

$$Y = 1 + \left(1 - 5 \times 10^{-6} u_0 d^* \frac{\rho_l}{\mu_l}\right) \left(1 - \frac{\theta}{2\pi}\right)$$

$$d^* = \max \left( d, 20 \left(1 - \frac{\rho_v}{\rho_w}\right)^{1/4} \left(\frac{0.06}{\rho_w - \rho_v}\right)^{1/2} \right)$$

**Contributions to the Pressure Gradient:**

$$\frac{dp}{dl} = \frac{dp_b}{dl} + \frac{dp_f}{dl} + \frac{dp_a}{dl}$$

*Pressure gradient due to gravity:*

$$\frac{dp_b}{dl} = (\alpha \rho_g + (1 - \alpha) \rho_l) g \sin \theta$$

*Pressure gradient due to acceleration:*

$$\frac{dp_a}{dl} = G^2 \left( \frac{x^2}{\rho_v \alpha} + \frac{(1-x)^2}{\rho_w (1-\alpha)} \right)$$

*Pressure gradient due to viscous losses:*

- Single phase:

$$\frac{dp_f}{dl} = \frac{2fG^2}{\rho d} \text{ where } f = \begin{cases} \frac{16}{\text{Re}} & \text{if Re} < 2000 \\ \frac{0.064}{\text{Re}^{0.2}} & \text{if Re} > 2000 \end{cases}$$

- Two phase, frictional pressure gradient (Lockhart-Martinelli):

$$\frac{dp_f}{dl} = \frac{1}{2} \left[ \left( \frac{dp}{dz} \right)_w \phi_w^2 + \left( \frac{dp}{dz} \right)_v \phi_v^2 \right]$$

$$\left( \frac{dp}{dz} \right)_w = \frac{2f[(1-x)G]^2}{d \cdot \rho_w} \quad \text{and} \quad \left( \frac{dp}{dz} \right)_v = \frac{2f(x \cdot G)^2}{d \cdot \rho_v}$$

$$X^2 = \frac{(dp/dz)_w}{(dp/dz)_v} \quad \phi_w^2 = \frac{(dp/dz)_F}{(dp/dz)_w} = 1 + \frac{C}{X} + \frac{1}{X^2} \quad \phi_v^2 = \frac{(dp/dz)_F}{(dp/dz)_v} = 1 + CX + X^2$$

### 21E.3 INTERPRETATION OF THE SULTAN EXPERIMENTS

The SULTAN tests were designed to investigate basic (separate-effects) aspects of boiling convection. In particular the effects of several key thermo-hydraulic (e.g. system pressure, heat flux, mass flow rate) and geometric parameters (e.g. channel dimensions) on pressure drop and critical heat flux (CHF) were systematically studied. These tests were conducted at the Grenoble Nuclear Research Centre (France/CEA/CENG) from 1994 to 1996. We make use here of the partial documentation available in the open literature (Rouge, 1997).

The overall facility is illustrated in Figure 21E.3-1a. The test section (Fig 21E.3-1.b) consists of a rectangular channel, heated from one of the side walls, and an outlet pipe. The heated side wall of the channel is a flat stainless steel plate 4 m x 0.15 m (13 ft x 5.9 in), and heat is supplied by the direct Joule effect. The distance between the heating side and the opposite wall, termed “gap”, was varied between  $\delta = 0.03$  m (1 in) and  $\delta = 0.15$  m (5.9 in). The cross-section hence varied from 0.15 m x 0.03 m (5.9 in x 1 in) to 0.15 m x 0.15 m (5.9 in x 5.9). The test section orientation was also changed from the vertical ( $\theta = 90^\circ$ ) to near horizontal ( $\theta = 10^\circ$ ) – with the heated side on top — to capture the effects of inclination. Data on pressure drop and CHF were obtained for: pressures  $p$ , 0.1-0.5 MPa (15-73 psia); inlet temperatures  $T_e$ , 50-150°C (120-300°F); mass flow velocities  $G$ , 5-4400 kg/m<sup>2</sup>s (1-901 lbm/s.ft<sup>2</sup>); and heat fluxes, 100-1000 kW/m<sup>2</sup> (8.8-88 Btu/s.ft<sup>2</sup>). We are interested here in the pressure drop measurements—besides these data being very appropriate to the inclined channels of the BiMAC, such information happens to be hardly available in previous two-phase pressure drop work.

In this section, our predictions of the pressure drop in the test section alone, and the total pressure drop including the outlet pipe, are evaluated against experimental data. Two sets of data were used for comparisons: (a)  $\theta = 90^\circ$  at  $p=0.5$  MPa (73 psia) with  $\delta = 0.03$  m (1 in), and (b)  $\theta = 10^\circ$  at  $p=0.5$  MPa (73 psia) with  $\delta = 0.15$  m (5.9 in). The results are summarized in Figures 21E.3-2 to 21E.3-7.

The Lockhart-Martinelli model appears to capture the general trend of the experimental data quite well. Calculations with  $s = 10$  and  $s = 40$  also yield good, in fact somewhat better predictions, especially for the low range of power levels which is of immediate interest here. This power dependency is as expected for the low inclination case—here we expect a stronger stratification, and/or slugging, with higher values of slip prevailing on the average.

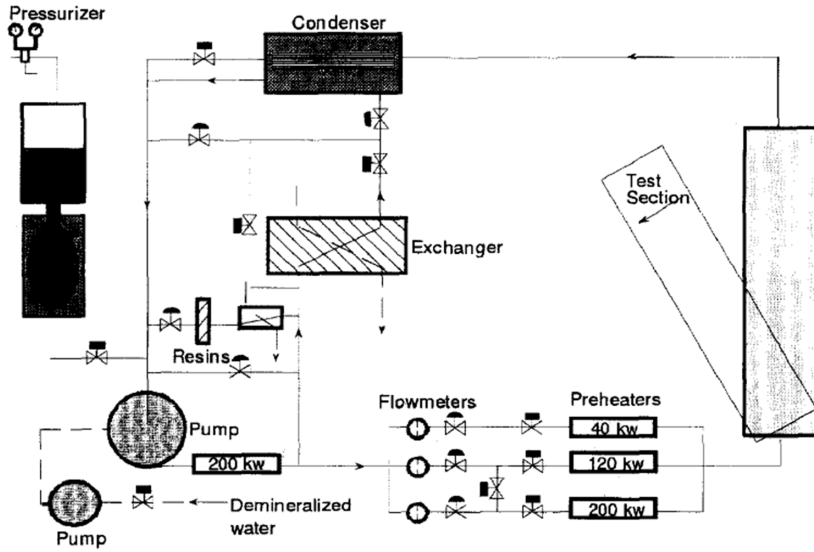


Figure 21E.3-1a. Schematic of the SULTAN Test Facility (Rouge, 1997)

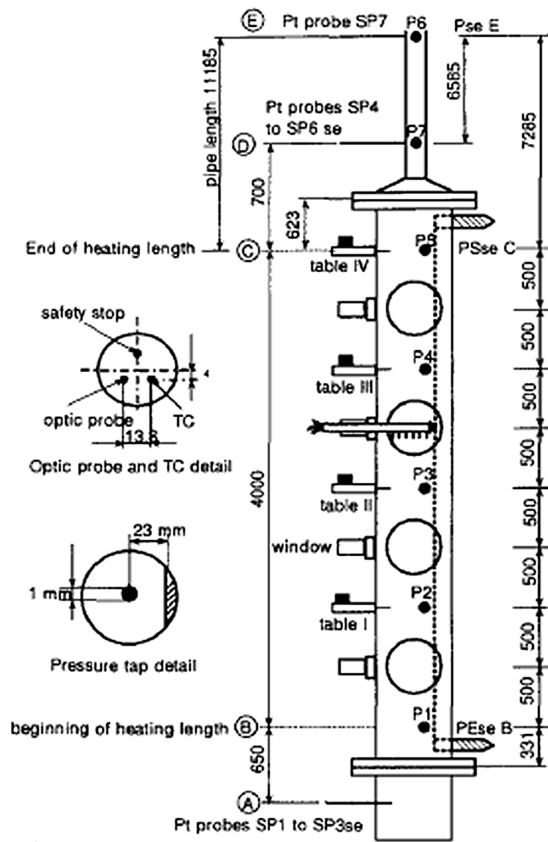
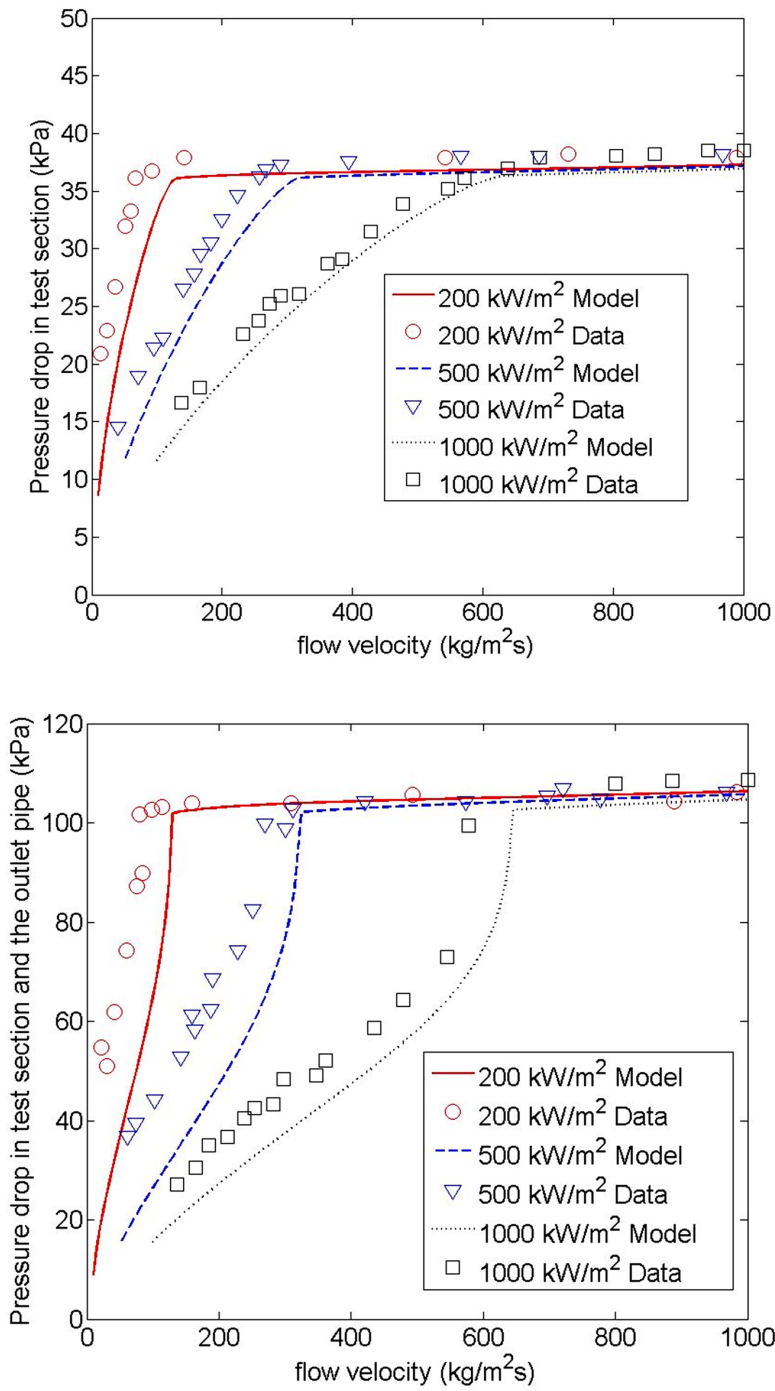
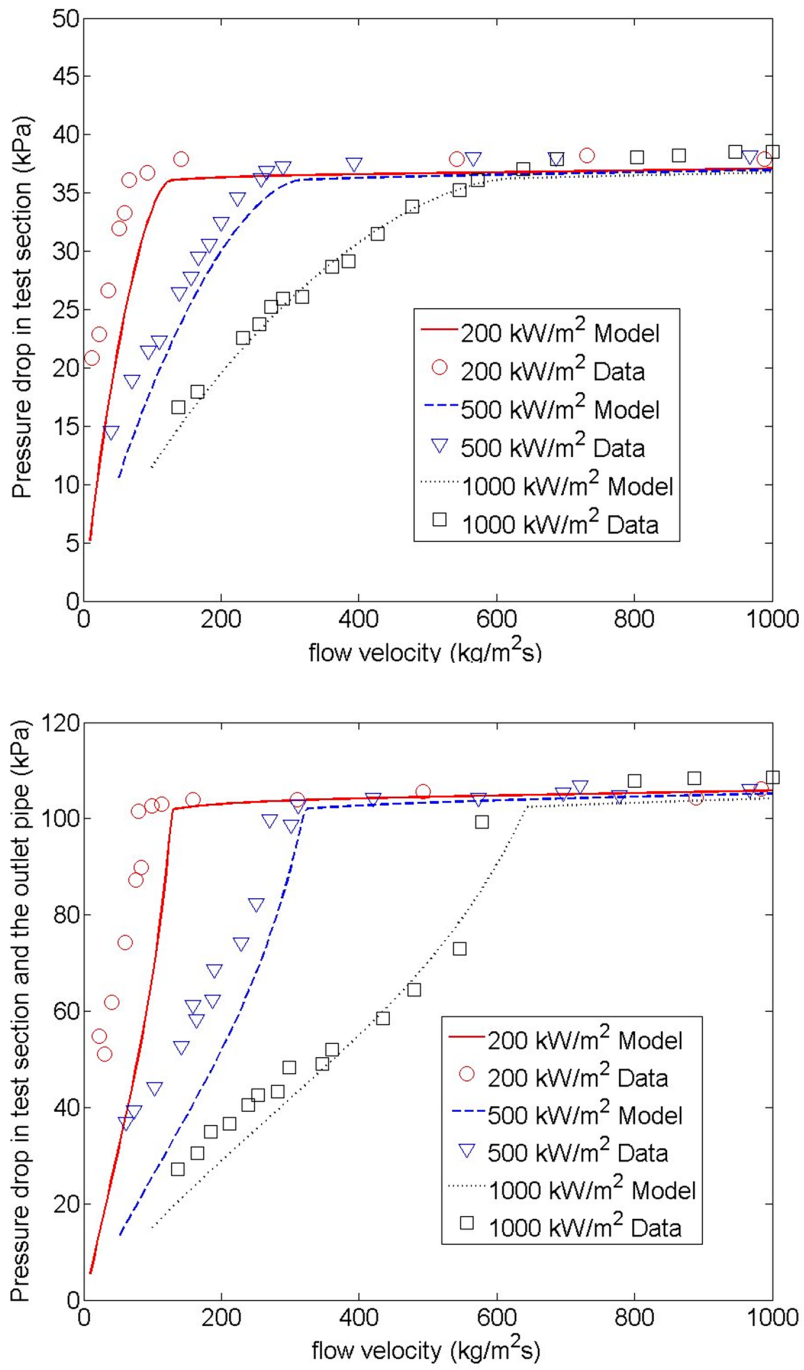


Figure 21E.3-1b. Illustration of the SULTAN test section (Shown in the vertical orientation)





**Figure 21E.3-2. Predictions of SULTAN Experiments**  
 ( $p = 0.5 \text{ MPa}$ ,  $\theta = 90^\circ$ ,  $\delta = 0.03 \text{ m}$ ,  $T_e = 100^\circ\text{C}$ ). Slip is given by L-M, Eq. (E.2)



**Figure 21E.3-3. Predictions of SULTAN Experiments**  
 ( $p = 0.5 \text{ MPa}$ ,  $\theta = 90^\circ$ ,  $\delta = 0.03 \text{ m}$ ,  $T_e = 100^\circ\text{C}$ ). Slip is set at  $s = 10$

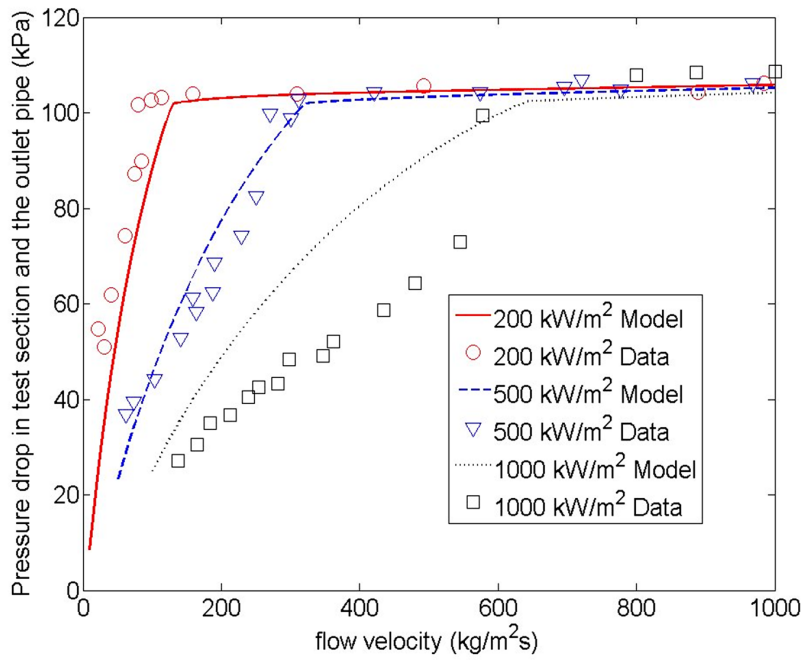
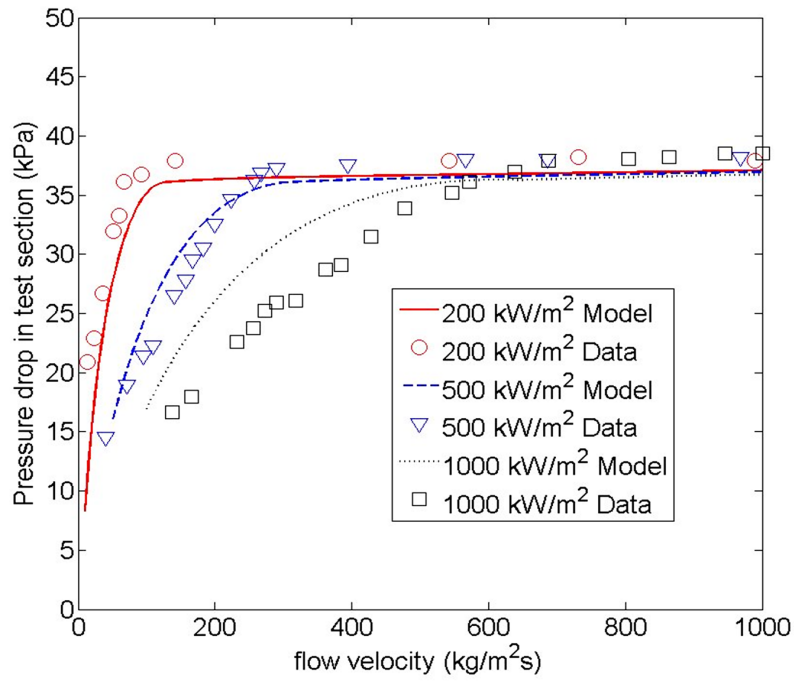


**Figure 21E.3-4. Predictions of SULTAN Experiments**  
 ( $p = 0.5 \text{ MPa}$ ,  $\theta = 90^\circ$ ,  $\delta = 0.03 \text{ m}$ ,  $T_e = 100^\circ\text{C}$ ). Slip is set at  $s = 40$

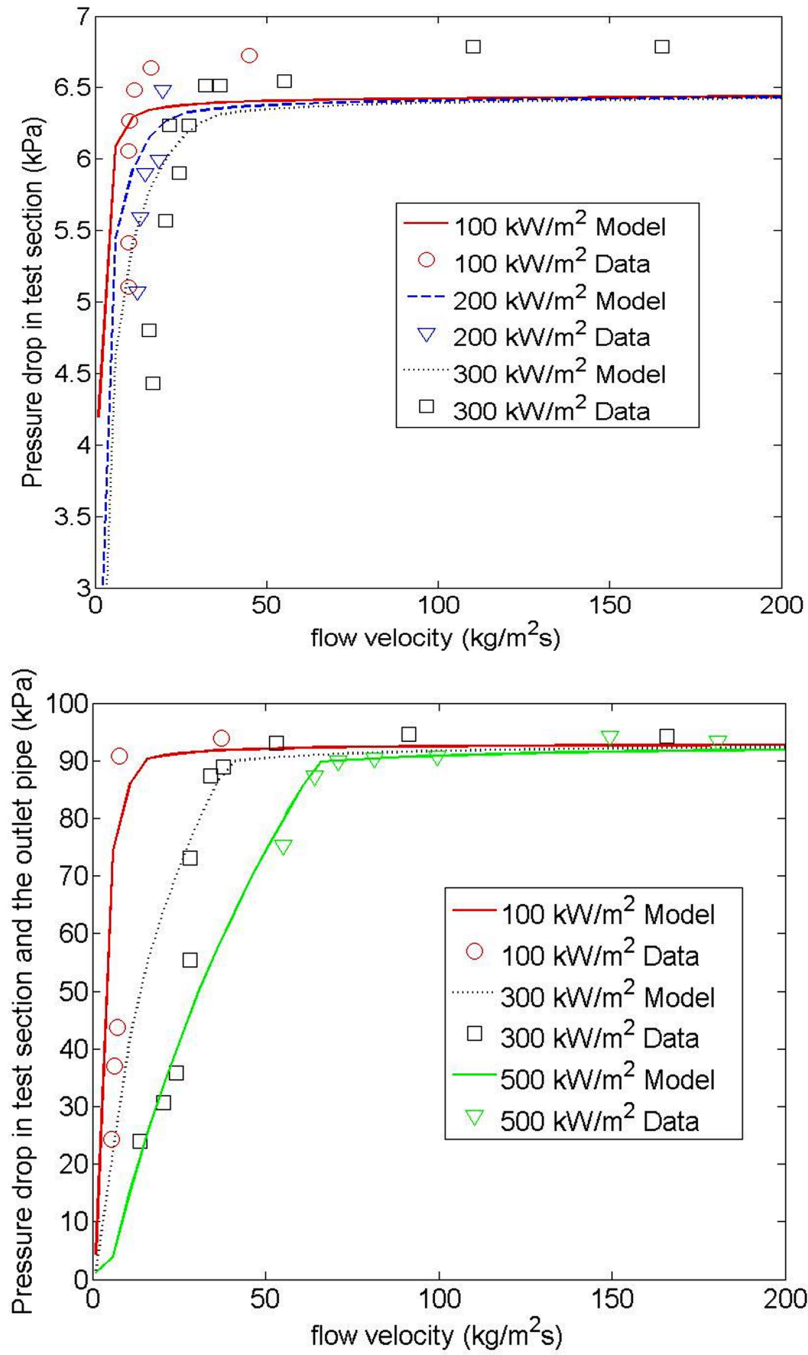


**Figure 21E.3-5. Predictions of SULTAN Experiments**  
 ( $p = 0.5 \text{ MPa}$ ,  $\theta = 10^\circ$ ,  $\delta = 0.15 \text{ m}$ ,  $T_e = 100^\circ\text{C}$ ). Slip is given by L-M, Eq. (E.2)

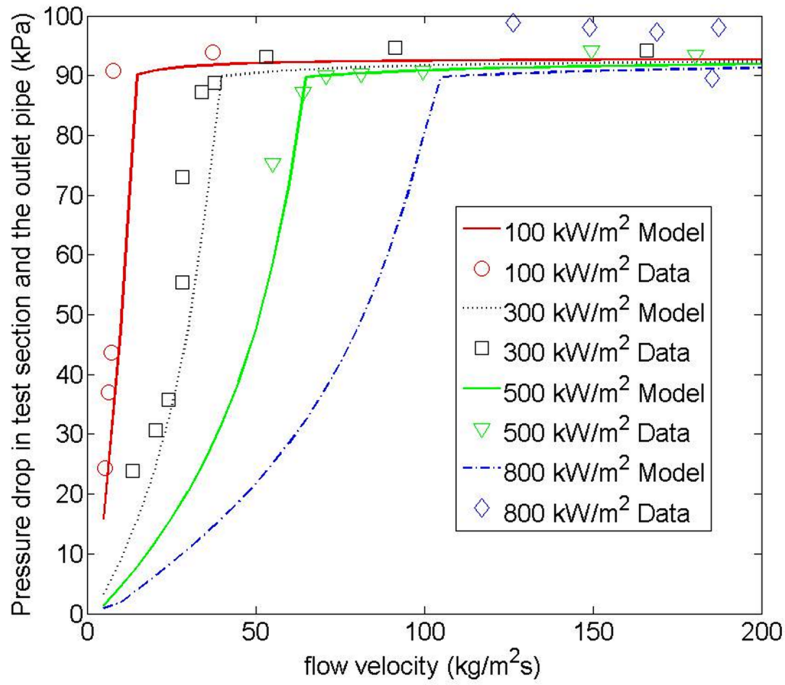
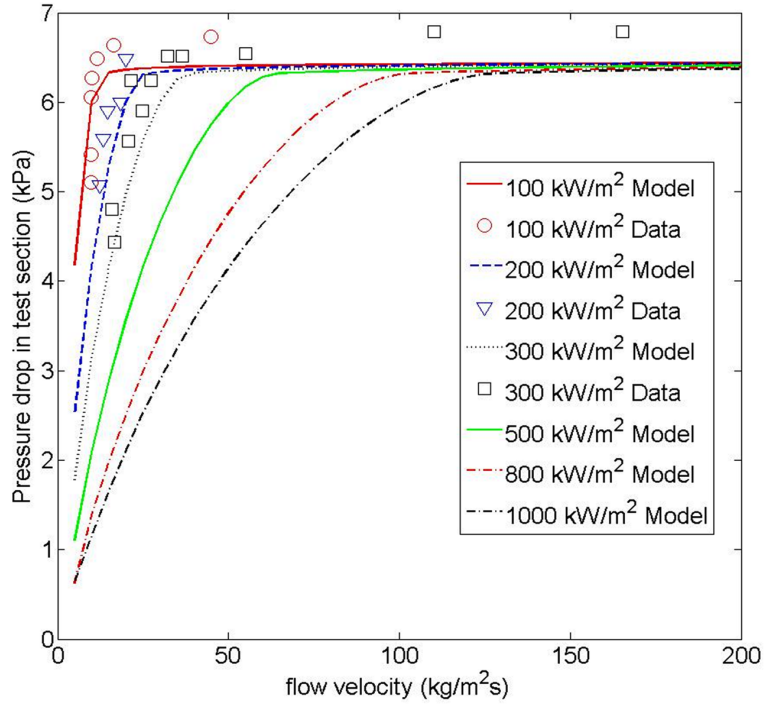


**Figure 21E.3-6. Predictions of SULTAN Experiments**  
 ( $p = 0.5 \text{ MPa}$ ,  $\theta = 100$ ,  $\delta = 0.15 \text{ m}$ ,  $T_e = 100^\circ\text{C}$ ). Slip is set at  $s = 10$

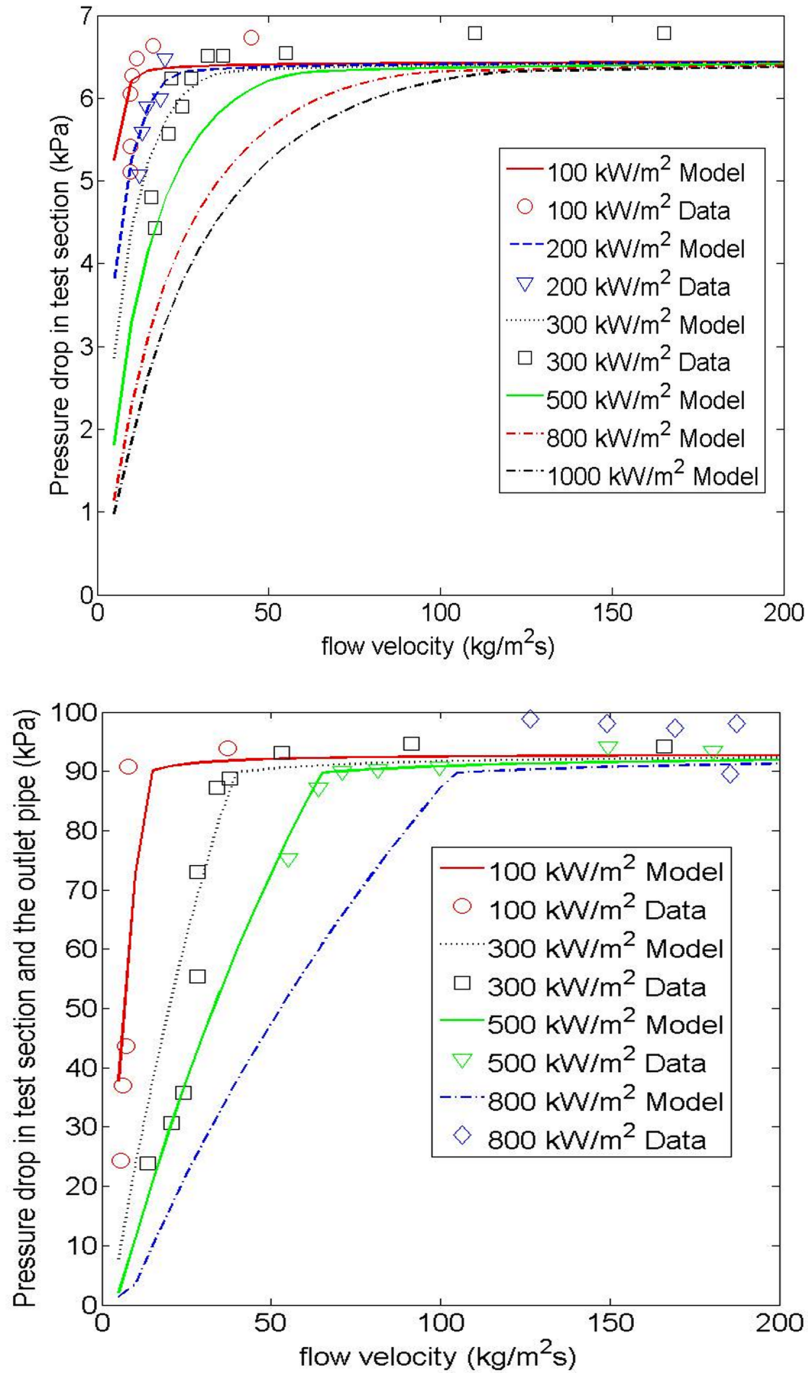


**Figure 21E.3-7. Predictions of SULTAN Experiments**  
 ( $p = 0.5 \text{ MPa}$ ,  $\theta = 10^\circ$ ,  $\delta = 0.15 \text{ m}$ ,  $T_e = 100^\circ\text{C}$ ). Slip is set at  $s = 40$

## 21E.4 TWO-PHASE NATURAL CIRCULATION FLOW IN THE BIMAC

As explained already in Section 21.5 (Subsection 21.5.4.4), one of the keys to the BiMAC fragility is the performance of two-phase natural circulation through its pipes. The basic question is whether there can be excursive, Ledinegg-type, instabilities due to two-phase losses that could starve the flow for long-enough periods of time to cause local dryouts, and perhaps temperature excursions that may be hard to recover in the natural circulation mode of BiMAC operation.

Here we examine the most limiting case for this type of concern, and that is the performance of the longest pipe thermally loaded all along its length. We use the Lockhart-Martinelli-based model described above for both pressure drops and void fraction calculations (Table 21E.2-1). Steady-state solutions are found by matching the pressure drop requirements in the loop to the pressure head made available by boiling. Different values of the power level are considered to cover the range of interest; they are applied uniformly over the length of the pipe. The effect of non-uniformity is also examined. All important dimensions are summarized in Table E21.4-1. Besides the flow rates, other important results of these calculations are the exit void fractions—they are needed to be sure there is enough liquid to keep the wall completely wetted. These results are presented in Figures 21E.4-1 (saturated water at the inlet), and Figures 21E.4-2 (10K (18°F) subcooling at the inlet). The effect of heated (pipe) length is shown in Figures 21E.4-3.

As we can see in Figure 21E.4-1a, for saturated water at the inlet, there is a broad maximum in flow rate, which in fact is around the range of heat fluxes of interest here ( $<100 \text{ kW/m}^2$  (8.8 Btu/s.ft<sup>2</sup>)). Moreover these results show that in this neighborhood, and even up to  $600 \text{ kW/m}^2$  (53 Btu/s.ft<sup>2</sup>) the gravity head dominates riser performance, so that the flow is self-adjusting, and self stabilizing—a decrease in flow would produce a more voided condition in the channel, and thus a driving force for an increase in flow. More specifically the “supply/demand” behavior for representative thermal loads on the BiMAC is shown in Figures 21E.4-4. We can see that the condition  $|\Delta P_R/dG| > |d \Delta P_D /d G|$  is satisfied, thus ensuring that any disturbances (of mass flow rate) do not escalate and rapidly return to the operating condition.

Finally, we must consider the size of downcomer flow area needed to supply all 100 pipes that make up the BiMAC jacket without significant pressure loss in the single-phase region of the flow loops. Sample results for an area of  $0.06 \text{ m}^2$  (0.6 ft<sup>2</sup>) feeding 30 and 60 pipes, at representative power loads are shown in Figures 21E.4-5. We can see that near-single pipe behavior can be obtained with rather modest downcomer flow area increases. The particular design choices will be subject to optimization, during the final design of BiMAC at the COL stage.

**Table 21E.4-1**  
**Geometric Parameters used in the BiMAC Flow Analyses**

Down-comer height/Diameter	1800/100 mm (71/3.9 in)
Down-comer horizontal section length/Diameter	5500/100 mm (220/3.9 in)
The riser length/Diameter	5000/100 mm (200/3.9 in)
The height of the vertical section of the riser	830 mm (33 in)



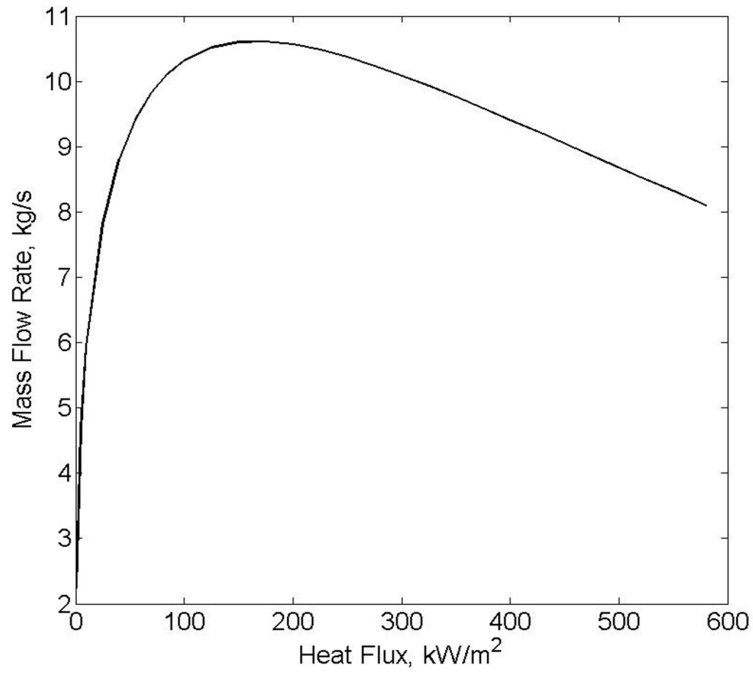


**Figure 21E.4-1a. Mass flow rate as function of applied heat flux.  $\Delta T_{sub}=0$**

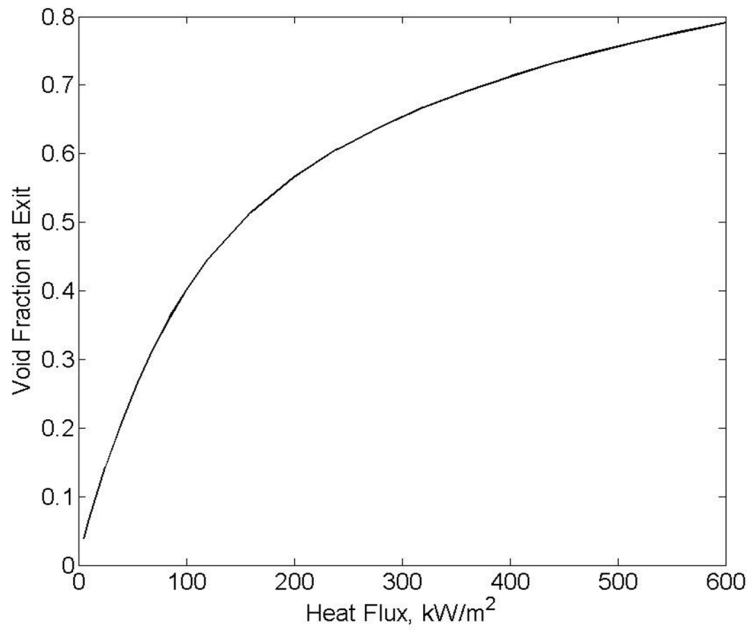


**Figure 21E.4-1b. Exit void fraction as function of applied heat flux.  $\Delta T_{sub}=0$**

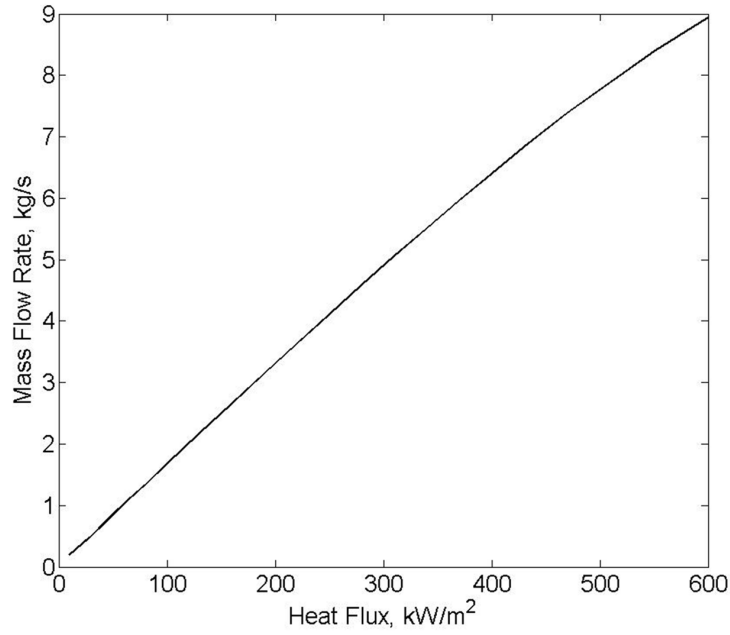


**Figure 21E.4-2a. Flow rate as function of applied heat flux.  $\Delta T_{sub}=10K$**

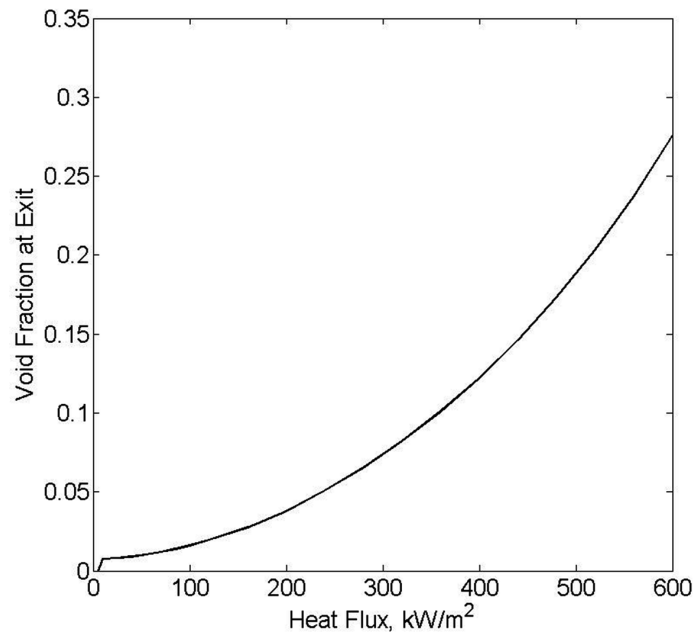


**Figure 21E.4-2b. Exit Void Fraction as Function of Applied Heat Flux K**

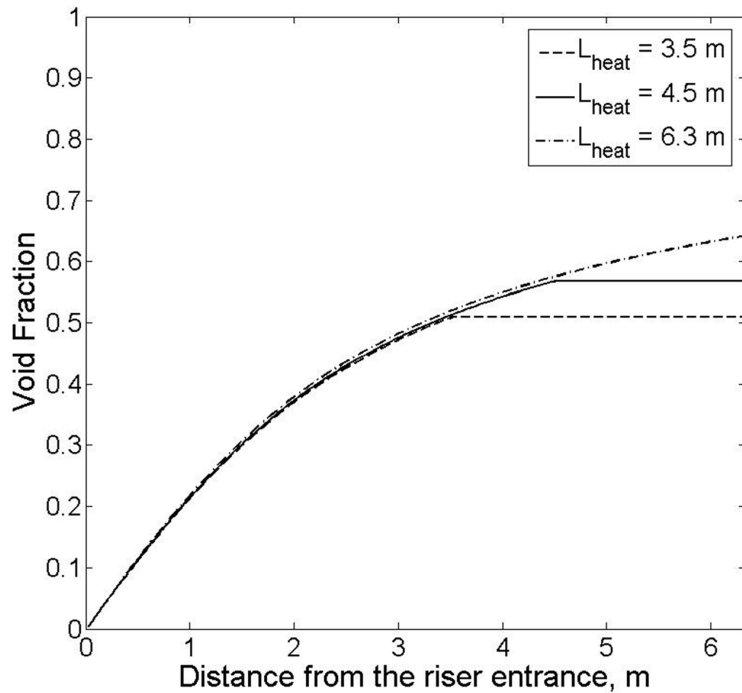


**Figure 21E.4-3. Riser Void Fraction Distribution as a Function of Heated Length**  
 Averaged heat flux  $200 \text{ kW/m}^2$ . The water is saturated at the entrance.

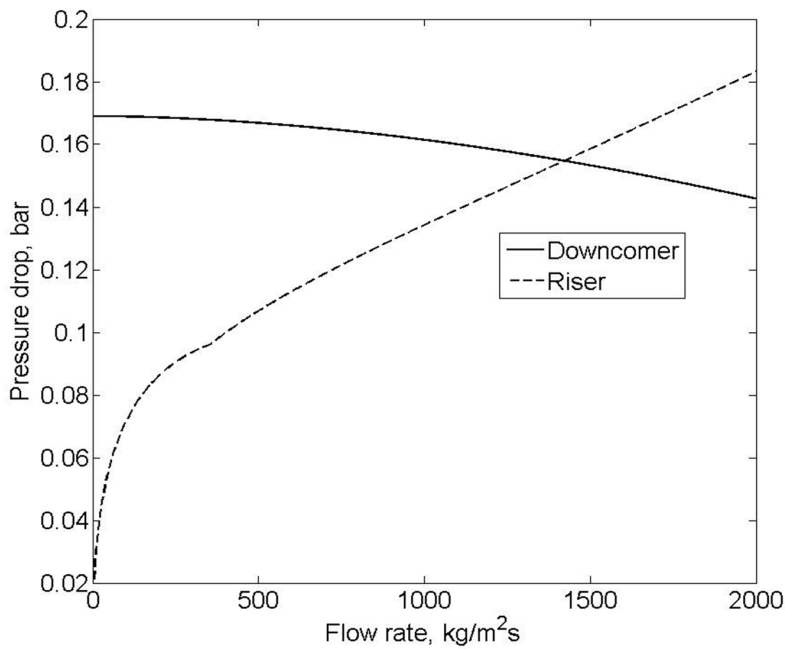


**Figure 21E.4-4a. Pressure Drop in the Downcomer and the Riser**  
 $(q = 100 \text{ kW/m}^2)$

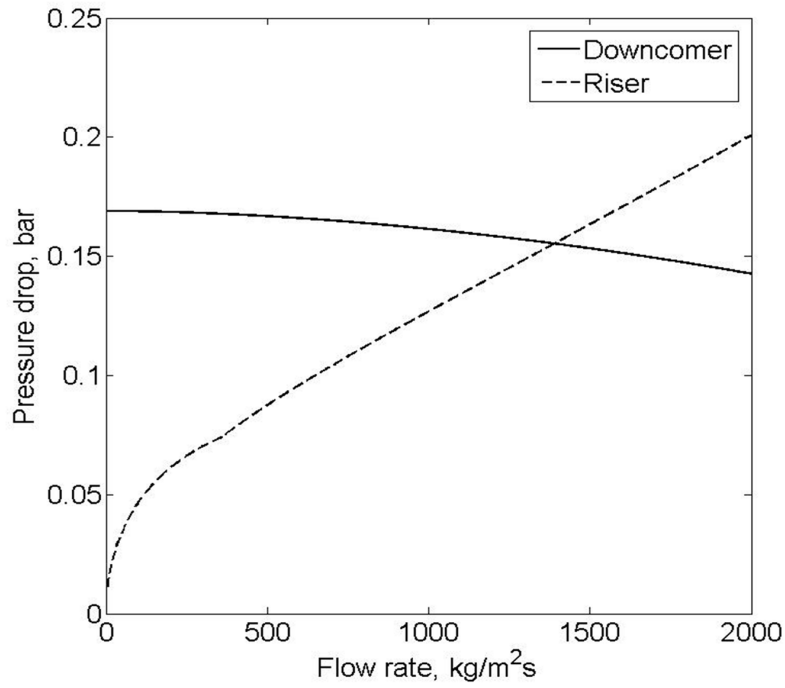


**Figure 21E.4-4b. Pressure Drop in the Downcomer and the Riser ( $q = 200 \text{ kW/m}^2$ )**

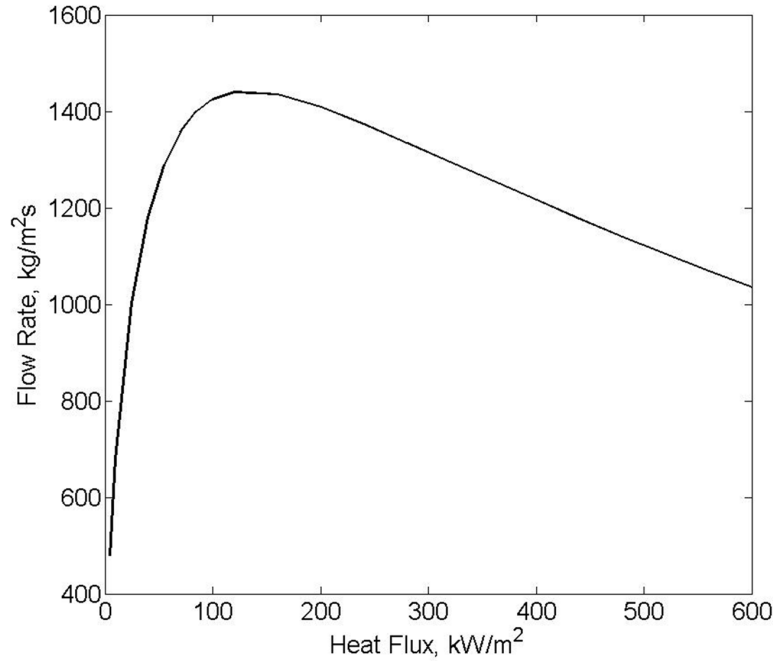


**Figure 21E.4-5a. Mass Velocity as Function of Applied Heat Flux**

Predictions of mass velocity as function of applied heat flux. Single-pipe loop with Downcomer flow area of  $0.06 \text{ m}^2$   $\Delta T_{sub} = 0. .$

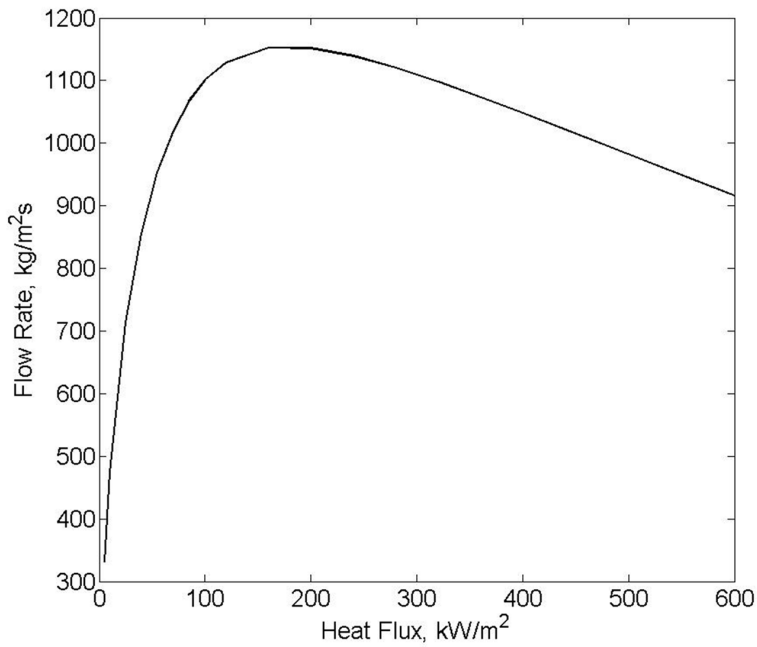


**Figure 21E.4-5b. Mass Velocity as Function of Applied Heat Flux**

Predictions of mass velocity as function of applied heat flux. A loop with 30-pipes for Riser and a Downcomer flow area of 0.06 m<sup>2</sup>  $\Delta T_{sub} = 0$  .

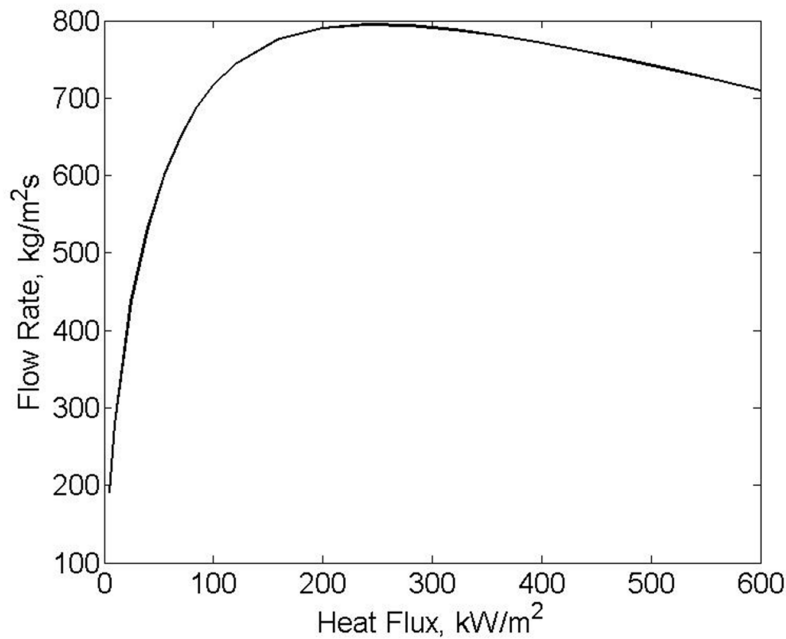


**Figure 21E.4-5c. Mass Velocity as Function of Applied Heat Flux**

Predictions of mass velocity as function of applied heat flux. A loop with 60-pipes for Riser and a Downcomer flow area of 0.06 m<sup>2</sup>  $\Delta T_{sub} = 0$  .

## 21E.5 CONCLUSIONS

We have shown that the pressure drop data obtained in the SULTAN facility are readily interpretable by means of a slip-equilibrium flow model using the Lockhart-Martinelli correlation for pressure drop and void fraction. This “benchmarking” is important because this experiment is matched quite well to the inclination and dimensions of a BiMAC channel, including that heating was supplied from above.

Applied to BiMAC, this model yields results that indicate stable operation under natural circulation conditions, while the flow and void fraction levels provide strong assurance that the heated wall would remain well wetted, and not be subject to dryouts. Moreover sample calculations show that the downcomer flow areas needed to supply the riser flows are rather modest: they will be subject to optimization, along with other BiMAC parameters during final design at the COL stage.

**Table 21E.5-1**  
**Nomenclature for Appendix 21E**

<b>Symbol</b>	<b>Description</b>	<b>Unit</b>
$D$	Hydraulic diameter of pipe	m (ft)
$F$	Friction factor	-
$G$	Mass flux	Kg/m <sup>2</sup> .s (lbm/s.ft <sup>2</sup> )
$L$	Length of pipe	m (ft)
$\dot{m}$	Mass flow rate	Kg/s (lbm/s)
$P$	Pressure	Pa (psi)
$Re$	Reynolds number	-
$S$	Slip ratio	-
$X$	Vapor (mass) quality	
$X_{tt}$	Lockhart-Martinelli parameter	-
$Y$	Coefficient	-
$Z$	Pipe length	m (ft)
$\alpha$	Void fraction	
$a_v$	Void fraction in vertical riser	-
$\beta$	Vapor volumetric flow ration	-
$\phi^2$	Two-phase friction multiplier	-
$\mu$	Viscosity	Pa.s (lbf.s/ft <sup>2</sup> )
$\theta$	Inclination angle of the riser	degree
$\rho$	Density	Kg/m <sup>3</sup> (lbm/ft <sup>3</sup> )
$\xi$	Coefficient	-
<b>Subscripts</b>		
$W$	Water	
$V$	Vapor	
$F$	Two-phase mixture	

**21E.6 References**

- 21E-1 Lin Z.H. (1992), "Characteristics of Gas-Liquid Two-Phase Flow In Pipelines and Their Engineering Applications," Xian Jiaotong Univ. Press.
- 21E-2 Lockhart R.W. and R.C. Martinelli (1949), "Proposed Correlation of Data for Isothermal Two-Phase Two-Component Flow in Pipes," Chem. Eng. Progr. 45, 39-48.
- 21E-3 Rouge, S. (1997). "SULTAN test facility for large-scale vessel coolability in natural convection at low pressure." Nuc. Eng. Des. 169: 185-195.
- 21E-4 Sneerova, P.I. A.P. Svare, E.L. Miropolski, Thermal Engineering, 1961, v.4 (reference [25] in Lin, 1992).
- 21E-5 Wallis, G.B. 1969. One-Dimensional Two-Phase Flow: McGraw-Hill, 51-54.